Continuous, fuel-cell-like operation of aluminum–air batteries via precipitate control and interfacial hydration

Yichao Shi,[1,2] Euigeol Jung,[1] Muqing Ren,[2] Xinyao Cai,[1] Jungtaek Kim,[1] Haoyu Wu,[1] and James H. Pikul[1]*

[1]Department of Mechanical Engineering, University of Wisconsin–Madison, Madison, WI, USA
[2]Department of Mechanical Engineering and Applied Mechanics, University of Pennsylvania, Philadelphia, PA, USA
*Correspondence: jpikul@wisc.edu

SUMMARY

Aluminum–air batteries offer high theoretical energy density and a safe, metal-based fuel, but practical deployments fail because of byproduct buildup, electrolyte fouling, and parasitic hydrogen evolution. We report a mechanically rechargeable Al–air cell that enables fuel-cell-like operation using three design choices: a porous anode pouch that prevents $Al(OH)_3$ from contaminating the hydrogel electrolyte, electrolyte microdosing to maintain water content and ionic conduction, and a compliant enclosure that preserves interfacial pressure while venting hydrogen. In 60 cm² cells with 1.5 mm thick Al, the system delivers 1.0 Ah cm^{-2} with 82% aluminum utilization and up to 3,260 Wh kg^{-1}_{Al}. Repeated anode swaps amortize hardware mass, yielding system-level energy densities up to 550 Wh kg^{-1}. In field tests, an Al–air-powered rover required 41% less battery mass than a Li-ion system to achieve the same range. This demonstrates a practical, field-serviceable Al–air power source for continuous, infrastructure-limited operation.

KEYWORDS

Metal–air battery, hydrogel electrolyte, mechanical rechargeability, hydrogen evolution reaction.

INTRODUCTION

Lithium-ion (Li-ion) batteries work well for electric vehicles, which only need moderate range and spend most of the day parked and available for charging. But a growing set of critical technologies operate under far more difficult constraints. A commercial quadruped robot typically runs for only ~90 minutes before needing an hour-long recharge,[1] which is unacceptable for continuous field or warehouse operation. A battery-electric excavator can carry a 300 kWh pack weighing over a ton and still cannot complete a full eight-hour shift of heavy excavation.[2] These systems use more energy than a Li-ion pack can practically supply, cannot wait hours to recharge, and often operate in locations with no reliable grid connection.[3-6] In these scenarios, Li-ion's strengths (high power, good cycle life, and reversible chemistry)[7-12] do not solve the core limitation: the energy in the battery runs out too quickly and electrical recharging is too slow or impossible.

Metal–air batteries are attractive in these settings because they offer extremely high theoretical energy densities and metal fuels that are easier to transport than conventional rechargeable packs. Recent work has shown that sodium–air batteries can operate in a fuel-cell-like mode, where molten sodium is continuously oxidized and the discharge product forms at the cathode, enabling steady removal of reaction products.[13] This architecture works for lithium and sodium systems because their oxides and peroxides form on the cathode side. However, the same strategy does not generalize to zinc (Zn), iron (Fe), or

aluminum (Al), where the oxidation product forms directly on the anode and accumulates at the reaction interface.[14] For these metals, passivation, precipitation, and interfacial blockage arise intrinsically from where the product forms, preventing true continuous operation and blocking any direct extension of the fuel-cell model. A different operating principle is required for long-duration use.

Aluminum–air (Al–air) batteries are particularly appealing because aluminum is inexpensive, energy-dense (8,100 Wh kg^{-1} of Al), abundant, and produces non-toxic, recyclable discharge products.[15-17] Aluminum is also inherently safe: it does not easily ignite, is not a hazardous material for transport, and is inexpensive to ship. Transporting power via aluminum costs on the order of $20 per MWh per 1,000 miles, compared to ~$120 for compressed hydrogen and ~$10,000 for Li-ion batteries (see Methods for calculations).[18-21] However, practical Al–air systems fail in predictable ways. Al oxidation generates large quantities of aluminum hydroxide ($Al(OH)_3$) precipitate that fouls electrolytes and block ionic pathways.[22] Electrolytes dry out and air-cathodes flood during multi-day operation.[23] Parasitic hydrogen evolution forms gas pockets that disrupt contact and waste active material.[22,23] Prior Al–air research has made important advances through component-level and materials-centered strategies,[15] including Al alloying and surface modification to improve utilization and manage the passivation layer,[24,25] modified electrolytes and additives to mitigate hydrogen evolution and improve stability,[26,27] and air-cathode or catalyst optimization to improve oxygen transport and reduce degradation.[28] Mechanical and fluidic strategies have also been explored, including oil-displacement layers that temporarily isolate the anode from the electrolyte during rest to suppress self-corrosion,[29] electrolyte-circulation systems that filter or dilute precipitates,[30] and spinning-cell architectures that use centrifugal force to expel $Al(OH)_3$ from the reaction interface.[31] These approaches improve specific failure modes and can enhance discharge capacity, energy density, or short-term stability, but they primarily optimize individual components or single-discharge operation. In addition, because electrochemical reduction of $Al(OH)_3$ back to Al remains impractical in conventional Al–air cells, Al–air batteries are generally operated as primary batteries rather than electrically rechargeable batteries.[16,22]

Mechanical replacement of consumed Al anodes has long been recognized as a way to extend Al–air operation without electrochemically recharging the cell.[16,32] For systems that must operate away from the grid, such as autonomous rovers, construction equipment, and disconnected data centers,[33-36] the inability to electrochemically recharge aluminum inside the discharge cell is not a disadvantage. These applications do not need to recharge in the operating cell; they need a power system that can run continuously as new fuel is supplied. Metal–air batteries can, in principle, operate like fuel cells in such scenarios, but only if fresh metal can be introduced and reaction products do not disable the cell. Achieving this for Al, Zn, or Fe requires a discharge architecture that can accept new anodes cleanly, remove accumulated discharge product, maintain ionic transport through an evolving product layer, vent hydrogen, preserve the electrolyte and cathode for reuse, and remain functional over multi-day operation. When these conditions are met, mechanical rechargeability—physically replacing the consumed aluminum—allows Al–air cells to operate in a fuel-cell-like manner, where fuel is continuously added and long-duration operation is limited only by the ability to supply aluminum or water.

Here, we approach mechanically rechargeable Al–air batteries as a coupled chemo-mechanical transport problem. Rather than treating $Al(OH)_3$ precipitation, electrolyte dehydration, hydrogen evolution, and interfacial contact loss as independent failure modes, we show that these processes are coupled transport and chemo-mechanical constraints that must be managed together to enable repeated discharge with thick Al anodes. This perspective leads to three mechanistically linked design principles. First, a porous, replaceable anode pouch confines the $Al(OH)_3$ precipitate near the anode, preventing it from fouling the reusable hydrogel electrolyte while still allowing electrolyte access to the Al surface and the evolving $Al(OH)_3$ layer. Unlike a conventional fixed separator,[37,38] the pouch fully encloses the anode and is removed together with the consumed Al anode and accumulated $Al(OH)_3$ during mechanical recharging, allowing the hydrogel electrolyte and air cathode to remain in the reusable cell hardware. Second, electrolyte microdosing regulates water and ion transport within the cell by maintaining hydrated ionic pathways through the growing $Al(OH)_3$ layer, compensating electrochemical water consumption, and preserving the hydration and integrity of the hydrogel electrolyte. Third, a spring-loaded cassette with patterned anode

perforations provides compliant mechanical stabilization: it accommodates anode-pouch swelling, maintains interfacial pressure, and expels hydrogen bubbles generated from the hydrogen evolution reaction (HER). In this way, hydrogen-bubble accumulation, interfacial contact, and the swelling of the $Al(OH)_3$ layer are managed as mechanically coupled processes at the cell scale. Together, these elements enable repeated thick-anode operation, stable multi-day discharge, and clean, rapid anode replacement.

Using 60 cm^2 cells with 1.5-mm thick Al anodes discharged at 10 mA cm^{-2}, this architecture delivers 1.0 Ah cm^{-2} capacity with 82% Al utilization and operates continuously through hundreds of ampere-hours. Because the hardware is reused across anode swaps, the effective system-level energy density increases with repeated discharge, reaching 550 Wh kg^{-1} after three cycles. We validate the approach in a field-deployed rover, where the total carried energy-storage mass, including reusable hardware, spent anodes, and microdosing electrolyte, was 41% lower than a range-matched Li-ion benchmark configured for the same 60-km mission.

The central contribution of this work is not a new chemistry but a functional, field-serviceable implementation of Al–air technology at meaningful scale. It demonstrates that, for robots and off-grid machines where carrying fuel is easier than installing chargers or hauling large battery packs, aluminum can be used as a safe, high-energy, easily transported power source.

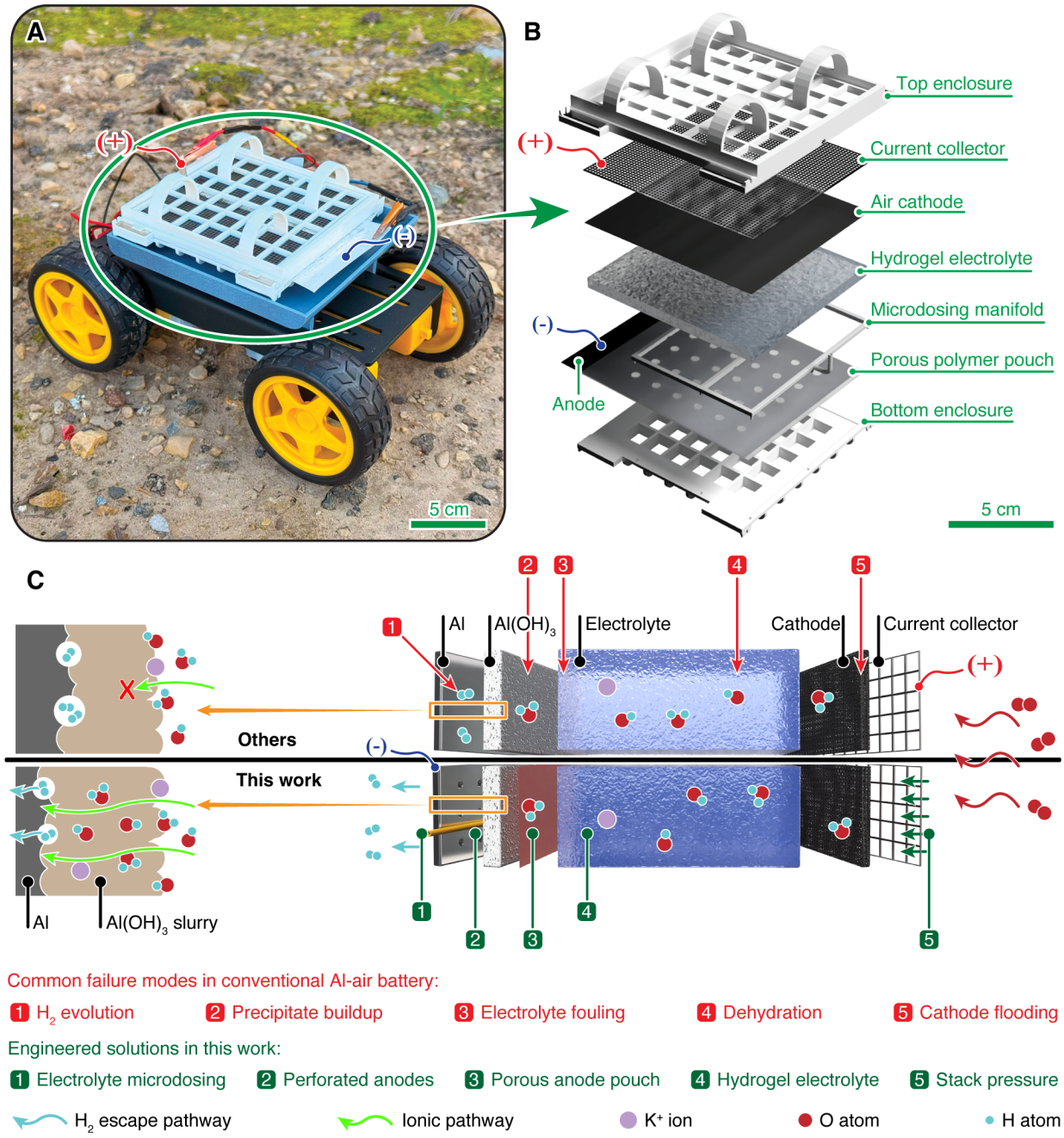


Figure 1. Architecture and design principles of a mechanically rechargeable Al–air battery

(A) The assembled Al–air battery powering an all-wheel-drive rover. (B) Exploded-view schematic illustrating the key components of the cell. (C) Comparison of failure modes in conventional Al–air cells (Others) versus our engineered cell architecture (This work). In conventional cells, $Al(OH)_3$ buildup, electrolyte fouling, dehydration, H_2 accumulation, and cathode flooding progressively block ionic transport and degrade performance. Our architecture addresses these coupled failure modes using a porous anode pouch, electrolyte microdosing, perforated anodes, a hydrogel electrolyte, and spring-loaded stack pressure.

RESULTS

Battery architecture and mechanical recharging process

Our mechanically rechargeable Al–air battery features a modular, 3D-printed enclosure with magnetic coupling for rapid, tool-free assembly, and consists of a single electrochemical cell (**Figure 1A**). As shown in the exploded view in **Figure 1B**, the internal stack of the cell consists of five key components arranged from cathode to anode: (1) a nickel mesh current collector, (2) a commercial carbon cloth air cathode with platinum (Pt) catalyst (4 mg cm^{-2}), (3) a hydrogel layer saturated with electrolyte solution (6 M potassium hydroxide (KOH) and 0.05 M potassium stannate (K_2SnO_3)), (4) a 3D-printed manifold for periodic electrolyte microdosing (**Figure S1**), and (5) a perforated Al anode enclosed in a porous polymer pouch. Together, these elements systematically address the common challenges of anode passivation, water management, and parasitic HER that limit conventional Al–air cells (**Figure 1C**).

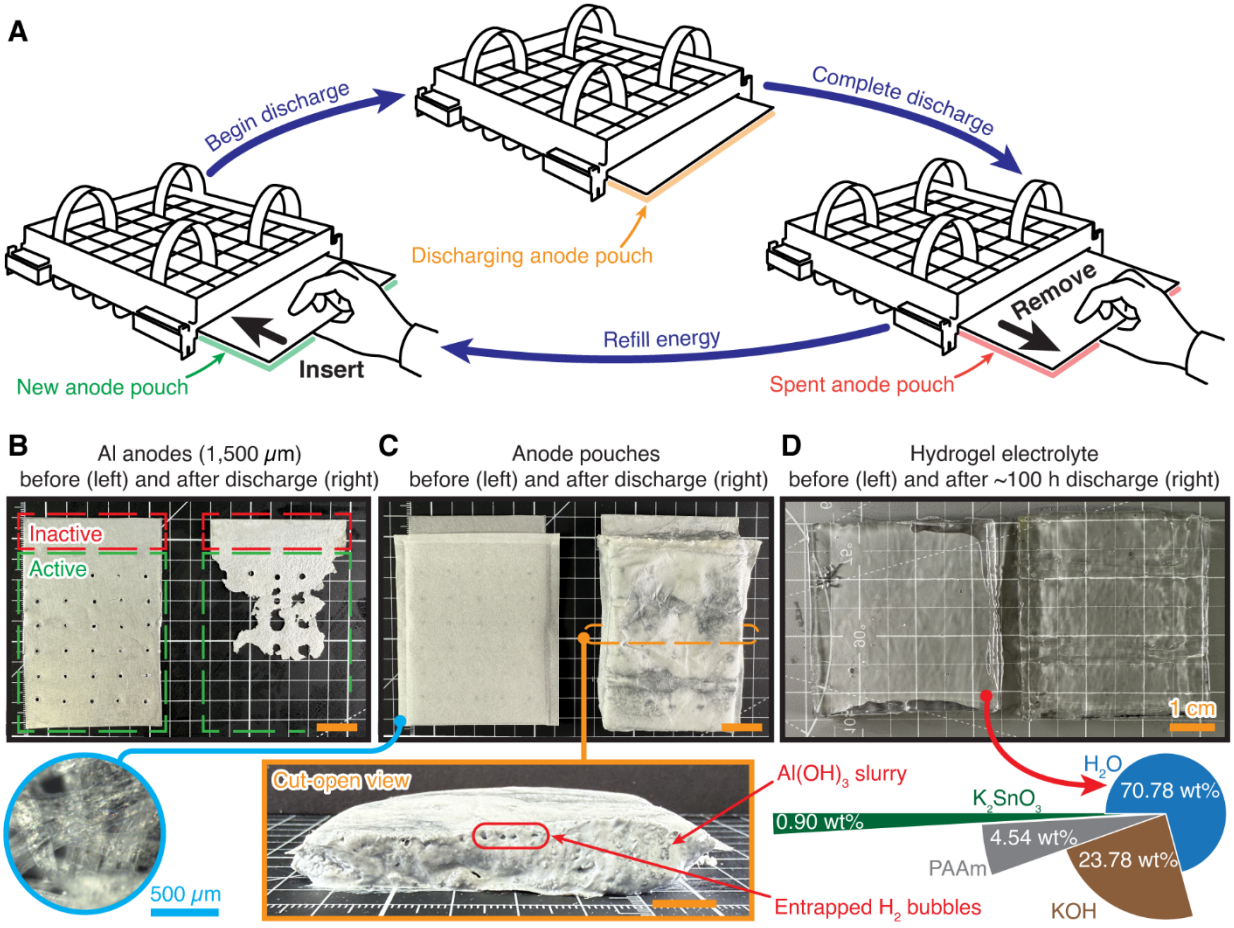


Figure 2. Mechanical recharging process and component evolution during discharge.
(A) Diagram of the mechanical recharging process, demonstrating the simple removal of the spent anode pouch and insertion of a fresh one. (B) 1.5 mm thick Al anodes before and after discharge, highlighting the inactive electrical contact tab and the electrochemically active region. (C) A photo of anode pouches before and after discharge. The cross-section reveals the contained $Al(OH)_3$ slurry. (D) Comparison of a fresh hydrogel electrolyte and a hydrogel after 100 hours of continuous discharge. The pie chart shows the mass composition of the fresh, electrolyte-saturated hydrogel.

This design enables a simple and rapid mechanical recharging process, visually detailed in **Figure 2A**. During discharge, the Al anode is consumed to form an $Al(OH)_3$ slurry, which is fully contained within the porous polymer pouch. To recharge, the spent anode and pouch are removed and a fresh anode and pouch are inserted. This exchange replenishes the battery's energy in under a minute and allows for immediate resumption of operation (**Supplementary Video S1**).

The Al anode is designed with two functional sections (**Figure 2B**): an active segment that is electrochemically consumed through Al oxidation and parasitic HER, and an inactive tab that provides a stable electrical connection. During discharge, Al in the active segment is converted into $Al(OH)_3$, producing substantial volume expansion and forming an ionically resistive passivation layer.

Compliant enclosure and hydrogen gas management

To accommodate the large volume expansion of the anode pouch while maintaining interfacial contact, the top enclosure was designed with a movable top face connected to the side frames by four curved springs. We characterized the spring response by vertically displacing the movable top face relative to the enclosure frame and converting the measured force–displacement behavior into an average stack pressure over the 60 cm² cell area (**Figure S2**). For cells assembled with 1.5 mm thick Al anodes, the internal stack initially deflects the movable top face by approximately 5 mm, generating an average stack pressure of 1.1–1.3 kPa. During discharge, the anode pouch swells further, and this expansion is accommodated by additional upward deflection of the movable top face. Based on the calibrated spring response, increasing the spring's total deflection to 10 mm corresponds to an average stack pressure of approximately 2.6 kPa. Thus, the spring-loaded enclosure does not impose a fixed pressure; instead, it provides a compliant pressure-regulation mechanism that accommodates pouch swelling while preserving contact among the anode pouch, hydrogel electrolyte, and cathode during long-duration discharge.

This compliant boundary condition is important not only for maintaining contact with a continuously swelling, mechanically evolving anode pouch, but also for managing gas accumulation at the Al–hydrogel interface. During discharge, parasitic HER continuously generates hydrogen bubbles, which can form interfacial voids and disrupt ionic contact if they are not removed. To guide gas release, the anode is patterned with a periodic array of perforations that serve as escape channels for hydrogen gas (**Figure 2B**). The maintained spring pressure and low gas permeability of the hydrogel electrolyte actively expel hydrogen bubbles through these perforations. Control experiments show that this coupled strategy of combining perforations with compression is more effective at preventing gas accumulation than using either feature alone (**Supplementary Video S2**). This synergy maintains uniform interfacial contact and prevents void formation even as the anode volume changes, thereby maximizing anode utilization efficiency.

Porous anode pouch for discharge-product confinement

Hydrogels offer advantages over liquid electrolytes in Al–air batteries, such as leak prevention, HER mitigation, and reduced CO_2 poisoning.[26,39-41] However, they face challenges from surface fouling. When the metal anode is directly in contact with the hydrogel, a thick, difficult-to-remove passivation layer of $Al(OH)_3$ forms directly on the hydrogel surface (**Figure S3**). This layer impedes ion transport, prevents effective contact when a fresh anode pouch is installed, and ultimately impairs the battery's mechanical rechargeability. Maintaining both the chemical composition and physical integrity of this hydrogel is critical for enabling continuous operation through repeated recharging. Our Al–air battery cell uses a polyacrylamide (PAAm) hydrogel consisting of 70.8 wt% water, 23.8 wt% KOH, 4.5 wt% PAAm, and 0.9 wt% K_2SnO_3. To evaluate its mechanical durability under alkaline electrolyte conditions, we subjected the hydrogel electrolyte to 500 compression cycles between 0% and 15% strain at 1 mm s^{-1}. The highly overlapping stress–strain curves indicate stable elastic recovery and negligible mechanical fatigue under repeated deformation, despite prolonged exposure of the PAAm network to the strongly alkaline electrolyte (**Figure S4**).

The porous polymer pouch in our cell design protects and extends the operational life of this hydrogel. Constructed from non-woven porous cloth, the polymer pouch captures $Al(OH)_3$ to avoid fouling of the hydrogel electrolyte and, being liquid-permeable, supports continued ionic conduction. While this

physical barrier introduces a modest resistance penalty, increasing internal resistance from 0.34 Ω to 0.51 Ω during initial discharge (**Figure S5**), this trade-off dramatically extends hydrogel lifetime and is essential for the cell's mechanical rechargeability. Without the pouch, the cell is limited to a single discharge; despite the initial benefit of lower internal resistance, the resulting interfacial fouling is so severe (**Figure S3**) that the cell cannot initiate a second discharge upon anode replacement.

The cut-open view of the spent anode pouch in **Figure 2C** shows that the accumulated $Al(OH)_3$ slurry is not a freely flowing liquid, but a concentrated paste-like slurry that is dense, mechanically cohesive, and can retain its shape against gravity. A fully discharged 1.5 mm thick Al anode forms a self-supporting paste approximately 8 mm thick. The applied stack pressure is low compared to the yield stress of similar pastes.[42] The pouch serves two functions: it permits electrolyte access to the Al surface while retaining the $Al(OH)_3$ slurry on the anode side and preventing direct contamination of the reusable hydrogel electrolyte.

This successful confinement is supported by cross-sectional scanning electron microscopy (SEM) images of dried pouches recovered at different depths of discharge. As discharge proceeds from approximately 30% to 60% and finally to 100% depth of discharge, the pouch interior becomes progressively filled with discharge product (**Figure S6A**). At full discharge, the Al anode is no longer visible in the pouch cross-section, and the pouch is instead occupied by $Al(OH)_3$ slurry, confirming that the discharge product accumulates locally within the pouch. X-ray diffraction (XRD) analysis of the corresponding spent anodes and recovered precipitates confirms that the retained solid is primarily $Al(OH)_3$ (**Figure S6B**).

Together, these macroscopic, microscopic, and crystallographic observations show that the pouch enables localized $Al(OH)_3$ containment. In addition to physically containing the discharge products, the pouch acts as a favorable nucleation scaffold for $Al(OH)_3$ precipitation. **Figure S7** shows the results of a precipitation experiment where we immersed the pouch material and hydrogel electrolyte in a supersaturated aluminate electrolyte solution. When immersed in supersaturated aluminate electrolyte, the pouch exhibited rapid $Al(OH)_3$ nucleation and growth and increased its mass by 8.6X after 2 hours in solution and 13X after 24 hours in solution. The hydrogels, in contrast, became slightly cloudy after 2- and 24-hour immersions but showed much less precipitation on them and a reduced mass likely due to some water loss from osmosis. These results indicate that the pouch does not simply retain reaction products after they form; rather, it promotes $Al(OH)_3$ precipitation at the pouch surface, thereby lowering the local $Al(OH)_3$ concentration near the hydrogel and helping preserve hydrogel function during discharge. This mechanism is consistent with our discharge experiments, where the hydrogel maintains ionic and physical contact with the pouch while exhibiting very low contamination after 100 h of discharge (**Figure 2D**).

The volume expansion associated with $Al(OH)_3$ precipitation becomes increasingly significant as anode thickness increases. For thin anodes up to 500 μm, the expansion is moderate, allowing the spent porous anode pouch to be slid out and replaced through the enclosure's front access slot. However, thicker anodes present a greater mechanical challenge. For 1,500 μm thick anodes, full discharge expands the pouch by 433% (**Figure 2C**). In such cases, the enclosure must accommodate the expansion and be opened to replace the expanded anode pouch, after which a new anode is inserted, and the corner magnets align the enclosure.

Microdosing

Electrochemical reactions, evaporation, and leakage result in water loss from the hydrogel, leading to progressive dehydration that manifests in two detrimental ways: (1) volumetric shrinkage, which disrupts interfacial contact and prematurely terminates discharge, and (2) increased surface tackiness, which causes adhesion and complicates mechanical recharging.[43-45] To compensate for water loss, the battery integrates a 3D-printed microdosing manifold that enables controlled periodic injection of fresh electrolyte solution (~60 μL cm^{-2} h^{-1}). This microdosing maintains hydrogel hydration, refreshes the Al–hydrogel interface, and provides lubrication for the extraction of the anode pouch after discharge. The effectiveness of this dual-protection approach is demonstrated in **Figure 2D** and **Supplementary Video S1**. Following 100 hours of continuous discharge with periodic anode replacement, the hydrogel electrolyte maintains its

original shape and remains free of $Al(OH)_3$ contamination, confirming the viability of long-term mechanical rechargeability.

Periodic microdosing, set at 30-minute intervals, is essential for sustained operation. Unlike conventional electrolyte replenishment or flow-cell operation,[46] the purpose of microdosing here is not to continuously flush the cell or maintain a large excess of free liquid electrolyte. Instead, microdosing provides a small, localized, and budgeted electrolyte input that maintains hydrogel hydration and ionic conduction through the discharge product while preserving the $Al(OH)_3$ precipitate as a confined paste-like slurry within the anode pouch. Thus, microdosing is used as an interfacial transport-regulation strategy rather than simple bulk electrolyte replacement.

At each injection, the solution flows into, and spreads across, the Al-hydrogel interface, and any excess not immediately consumed or absorbed drains into an underlying reservoir for reuse in subsequent injections. Determining the optimal injection volume requires understanding the system's water flow pathways (**Figure 3A**). Water is added to the system from the microdosing manifolds and by water stored in the hydrogel. Water is consumed through four pathways: (1) the oxygen reduction reaction (ORR, $4Al + 3O_2 + 6H_2O \rightarrow 4Al(OH)_3$), (2) parasitic HER ($2Al + 6H_2O \rightarrow 2Al(OH)_3 + 3H_2$), (3) hydration of the $Al(OH)_3$ slurry, and (4) leakage to the environment. This environmental loss includes both evaporation to ambient air and gravity-driven minor liquid leakage. To quantify the passive dehydration component under the ambient testing conditions, we placed an electrolyte-loaded hydrogel on a balance at ~24 °C and ~45% relative humidity for 144 h and tracked its mass loss (**Figure S8**). The mass loss corresponded to an average evaporation rate of ~2 μL cm^{-2} h^{-1}. Because the hydrogel was directly exposed to ambient air during this test, this measurement provides a conservative upper-bound estimate of passive evaporation during battery operation, where the hydrogel is enclosed within the battery casing. The $Al(OH)_3$ slurry's hydration is critical for maintaining an ionically conductive pathway throughout the cell stack, which enables continued oxidation at the underlying Al surface and ensures uniform utilization of the full anode thickness.

To quantify the effect of microdosing flow rate on performance, we tested four batteries with 1,500 μm-thick anodes at 10 mA cm^{-2} (**Figure 3B**). Without microdosing, the battery relied solely on the hydrogel's water and delivered only 0.10 Ah cm^{-2}. Introducing microdosing dramatically improved areal capacity: a net injection rate of 30 μL cm^{-2} h^{-1} yielded 0.54 Ah cm^{-2}, and 60 μL cm^{-2} h^{-1} achieved 0.99 Ah cm^{-2}. Sufficient electrolyte replenishment ensured the resulting $Al(OH)_3$ layer remained ionically conductive, allowing for efficient utilization of the underlying anode; however, increasing the rate to 160 μL cm^{-2} h^{-1} yielded only a marginal capacity increase (from 0.99 to 1.00 Ah cm^{-2}) indicating the anode was almost fully utilized with the 60 μL cm^{-2} h^{-1} dosing. Based on a theoretical capacity of 1.21 Ah cm^{-2} (for 1,500 μm Al), these results correspond to anode utilization efficiencies of 8.3% (no dose), 44.6% (30 μL cm^{-2} h^{-1}), and over 82% (60 and 160 μL cm^{-2} h^{-1}). Notably, the galvanostatic discharge profiles exhibit a small, sawtooth-like pattern, with sharp periodic voltage fluctuations synchronized with each 30-minute microdosing event (**Figure 3B**, Inset), superimposed on an otherwise standard voltage–capacity curve.

Beyond enhancing capacity, microdosing is critical for preserving the hydrogel by managing the system's water and electrolyte balance, as quantified by the Sankey diagrams in **Figure 3C**. These diagrams illustrate the grams of water attributed to each process per ampere-hour of aluminum capacity delivered. Following the magnitude of each color-coded process as the microdosing increases (left to right) shows how the added microdosing shifts the primary water source from the hydrogel to microdosing. Without microdosing, the hydrogel is the sole water supplier and is rapidly depleted, losing 2.18 g of electrolyte for every ampere-hour of capacity delivered. With microdosing, the injected electrolyte via microdosing becomes the primary water source, and the hydrogel's contribution drops to just 0.10 g Ah^{-1} (at 60 μL cm^{-2} h^{-1}) and 0.03 g Ah^{-1} (at 160 μL cm^{-2} h^{-1}).

Microdosing also affects other water pathways. For each ampere-hour of capacity, the cathode electrochemical reaction consumes a constant 0.34 g of water. Higher microdosing volumes increase discharge capacity and, therefore, the amount of electrolyte absorbed by the additional $Al(OH)_3$ slurry to

maintain ionic pathways. While microdosing slightly increases parasitic HER, this effect plateaus at higher injection volumes. The unrecovered H_2O and KOH is highest in the no-dose case (1.39 g Ah^{-1}), an effect amplified by its extremely low total capacity. For the microdosing-enabled cases, the loss rate shows a positive correlation with dosing volume, rising from 0.06 g Ah^{-1} (at 30 µL cm^{-2} h^{-1}) to 0.38 g Ah^{-1} (at 160 µL cm^{-2} h^{-1}), likely because a wetter system is more prone to evaporation. Importantly, these measurements show that ~38% of the added water is needed to sustain ionic conductivity in the evolving $Al(OH)_3$ product layer, about 47% more water than what is needed for the oxygen reduction reaction in the 60 µL cm^{-2} h^{-1} discharge. Taken together, the 60 µL cm^{-2} h^{-1} regimen represents the optimal rate: it maximizes anode utilization while effectively minimizing hydrogel degradation and electrolyte waste and was therefore selected for subsequent discharge experiments.

Impedance evolution during discharge

To evaluate how microdosing affects the ionic conductivity during discharge, we monitored the cell impedance by electrochemical impedance spectroscopy (EIS) for cells operated with and without electrolyte microdosing (**Figure 4A,B**). In both cells discharged at 10 mA cm^{-2}, the areal power density remained relatively stable through most of the discharge, averaging 13.61 ± 0.14 mW cm^{-2} without microdosing and 13.98 ± 0.48 mW cm^{-2} with microdosing when the final 5% terminal discharge region was excluded. After discharge, both cells showed an increase in ohmic resistance and charge-transfer resistance. For the cell without microdosing, the ohmic resistance increased from 0.21 to 0.28 Ω, while the charge-transfer resistance increased from 0.32 to 0.85 Ω. For the microdosed cell, the ohmic resistance increased from 0.17 to 0.43 Ω, while the charge-transfer resistance increased from 0.44 to 0.69 Ω. While these results indicate that both cells experience impedance increase during discharge, the cause differs between the two systems. Without microdosing, the resistance increase is attributed to the accumulation of an $Al(OH)_3$ passivation layer that blocks ionic pathways and terminates discharge before complete anode utilization. Consistent with this interpretation, cells without microdosing delivered only ~6 Ah before excessive interfacial resistance stopped discharge, regardless of the Al anode thicknesses being 250, 500, or 1,500 µm. In contrast, electrolyte microdosing preserved hydrated ionic pathways within the evolving $Al(OH)_3$ layer, thereby delaying impedance growth and sustaining power output over longer discharge times. During the main discharge period of the microdosed cell, the fitted charge-transfer resistance remained nearly unchanged, increasing only from 0.44 to 0.48 Ω over 15.5–76.3% depth of discharge. This resistance stability explains the stable power output of the microdosed cell during long-duration discharge, allowing the 500 µm Al anode cell to deliver nearly 20 Ah. The final increase in charge-transfer resistance occurred only after the 500 µm Al anode was fully consumed in the microdosed cell.

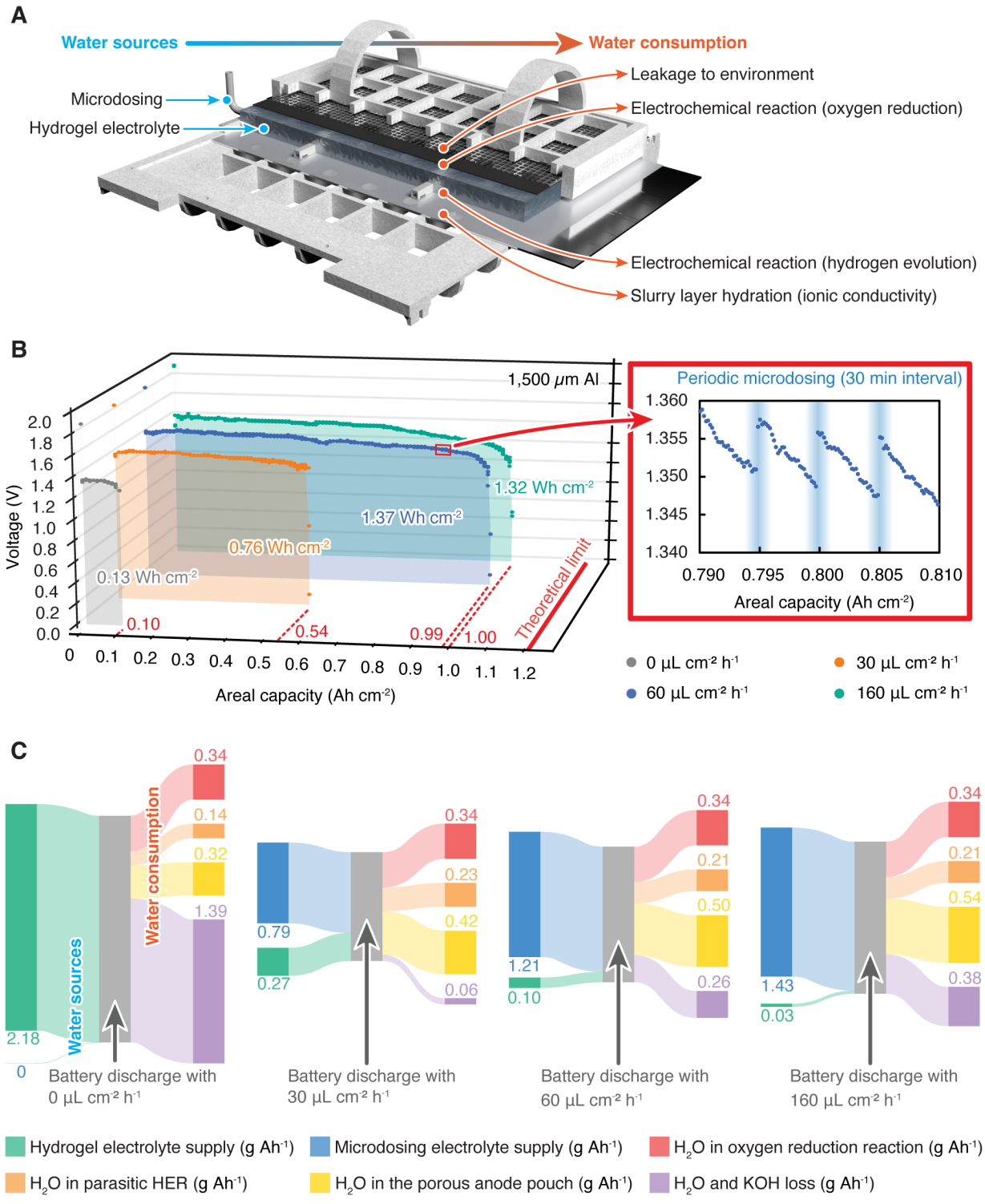


Figure 3. Water flow and electrolyte microdosing

(A) Schematic of water sources and sinks within the cell. (B) Galvanostatic discharge curves for batteries using 1,500 μm thick anodes under different microdosing flow rates (0, 30, 60, and 160 μL cm^{-2} h^{-1}), with inset showing the sawtooth-like voltage pattern from periodic microdosing. (C) Sankey diagrams quantifying the mass balance of water and electrolyte per ampere-hour of discharge, under different microdosing conditions.

Electrolyte formulation

The electrolyte formulation influences both the Al oxidation and HER rates. While 6 M KOH was selected for its high ionic conductivity, it is also known to accelerate corrosion and HER.[47,48] To mitigate this, we investigated adding 0.05 M K_2SnO_3, a known HER suppressor.[27,49] The HER-mitigation role of K_2SnO_3 is consistent with prior reports that stannate species form a protective metallic tin (Sn) layer on Al surfaces, increasing the HER overpotential and reducing direct contact between Al and electrolyte. To verify that this stannate-derived deposition also occurs in our mechanically rechargeable cell, we performed XRD on discharged anodes collected at different depths of discharge. The consistent metallic Sn peaks observed at ~30%, ~60%, and ~100% depth of discharge indicate that stannate-derived Sn deposition occurs during operation in our system (**Figure S6C**).

We compared the performance of batteries with 250 μm and 500 μm anodes using hydrogels with and without the stannate additive (**Figure 4C**). The inclusion of K_2SnO_3 yielded a substantial performance improvement. With the stannate additive, doubling the anode thickness from 250 μm to 500 μm resulted in a proportional, twofold increase in areal capacity (0.16 to 0.33 Ah cm^{-2}). Al-specific capacity and Al-specific energy, normalized by the mass of the electrochemically active Al region of the anode, remained high and stable (2350–2430 Ah kg^{-1}_{Al} and 3080–3260 Wh kg^{-1}_{Al}), indicating efficient anode utilization. In sharp contrast, the KOH-only electrolyte exhibited a sub-linear capacity increase (0.12 to 0.19 Ah cm^{-2}) and a severe performance decline with the thicker anode: Al-specific capacity dropped from 1800 to 1390 Ah kg^{-1}_{Al} and Al-specific energy fell from 2070 to 1510 Wh kg^{-1}_{Al}.

This enhancement is further corroborated by continuous discharge tests over three mechanical recharges (**Figure 4D**). The stannate-containing electrolyte produced flatter voltage profiles, higher cumulative capacity, and more stable power output across sequential anode replacements. For 250 μm anodes, the average power in the KOH-only electrolyte decreased from 14.5 ± 0.5 mW cm^{-2} in the first discharge to 10.6 ± 0.9 mW cm^{-2} in the third discharge, whereas the stannate-containing electrolyte maintained power from 14.5 ± 0.2 mW cm^{-2} to 14.0 ± 0.2 mW cm^{-2}. A similar trend was observed for 500 μm anodes: the KOH-only electrolyte decreased from 13.9 ± 0.6 mW cm^{-2} to 7.3 ± 0.8 mW cm^{-2}, while the stannate-containing electrolyte maintained substantially higher power from 13.9 ± 0.2 mW cm^{-2} to 13.1 ± 0.3 mW cm^{-2}. Additionally, the stannate-containing electrolyte increased the cumulative capacity over three 500 μm anodes by 79% compared with the KOH-only electrolyte (58.9 Ah vs. 32.8 Ah). These results confirm that the stannate additive is crucial for maintaining a reactive and stable anode interface; therefore, 6 M KOH with 0.05 M K_2SnO_3 was established as the standard electrolyte.

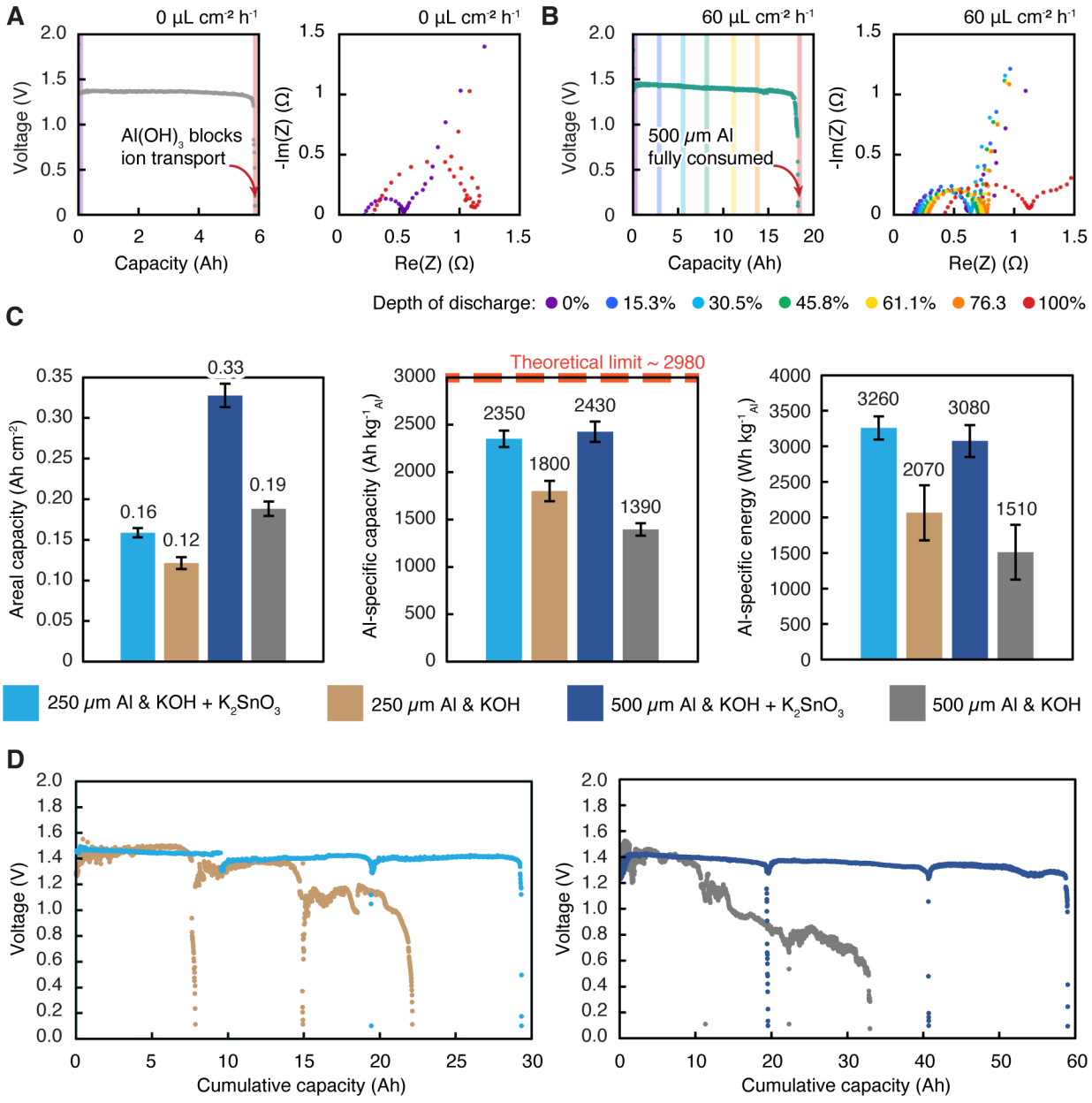


Figure 4. Effect of microdosing and electrolyte additives on battery performance and failure. (A) Galvanostatic discharge curve and corresponding Nyquist plots for a cell using a 1,500 µm Al anode without electrolyte microdosing. EIS was measured at the beginning of discharge and near the end of discharge. (B) Galvanostatic discharge curve and corresponding Nyquist plots for a microdosed cell using a 500 µm Al anode. EIS was measured at multiple depths of discharge, including 0%, 15.3%, 30.5%, 45.8%, 61.1%, 76.3%, and 100%. (C) Areal capacity, Al-specific capacity, and Al-specific energy for batteries with 250 and 500 µm Al anodes in 6 M KOH with and without 0.05 M K_2SnO_3. (D) Continuous discharge curves of sequential anodes comparing the two electrolytes.

333

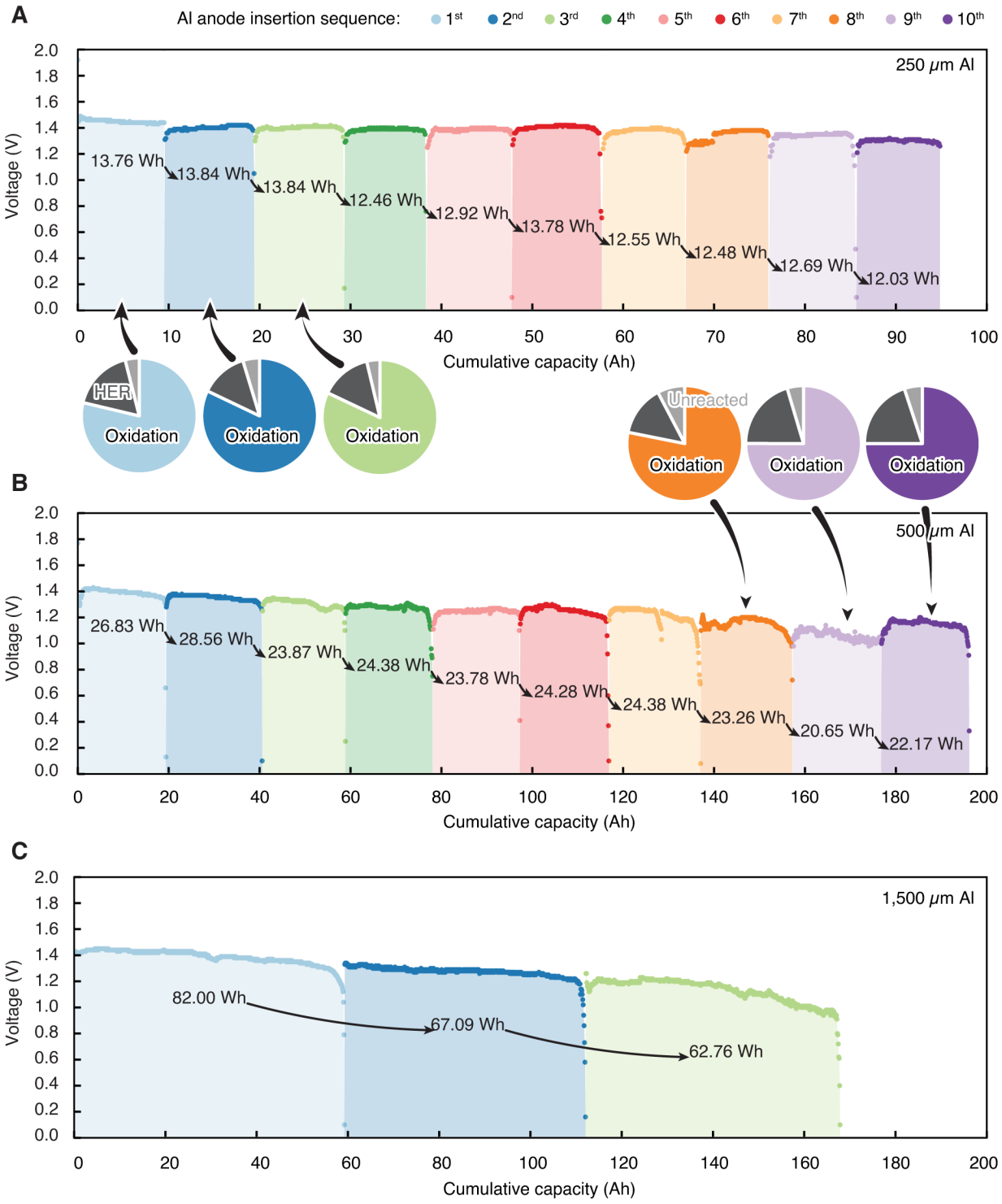


Figure 5. Mechanical rechargeability of Al–air batteries.
(A–C) Sequential discharge profiles for batteries with 250 μm, 500 μm, and 1,500 μm anodes. Pie charts indicate Al utilization pathways (electrochemical oxidation, HER, and unreacted Al) for representative discharges.

334

Electrochemical characterization and mechanical rechargeability

To evaluate the robustness and long-term durability of the mechanical recharging system, we performed sequential discharge experiments using 250, 500, and 1,500 μm Al anodes. In each test, a spent anode pouch was replaced with a fresh one while retaining the same enclosure, air cathode, and hydrogel electrolyte. The system showed excellent performance and stability across multiple discharges. Batteries with 250 μm anodes completed ten consecutive discharges, achieving a cumulative capacity of 95.6 Ah (**Figure 5A**). The energy output per anode was remarkably consistent, declining by only 12.6% from the first (13.76 Wh) to the tenth (12.03 Wh) discharge. Doubling the anode thickness to 500 μm yielded a correspondingly higher energy output (20.65–28.56 Wh per discharge) and a cumulative capacity of 196.20 Ah over ten discharges (**Figure 5B**). The 1,500 μm anodes delivered the highest energy per discharge, producing 82.00, 67.09, and 62.76 Wh over the first three discharges, respectively, demonstrating that even thick anodes can be effectively utilized (**Figure 5C**).

Compositional analysis of consumed anodes (**Figure 5A,B**, pie charts) revealed that electrochemical oxidation was the dominant process (75–80% of Al utilization), while parasitic HER consumed 15–18% and only 5–7% of aluminum remained unreacted. Despite this high efficiency, a gradual voltage decay was observed over prolonged operation (12–14 days for **Figure 5B,C**), particularly for thicker anodes. This decline is attributed to slow-onset degradation mechanisms, including cathode flooding and minor hydrogel surface fouling. Consistent with this interpretation, EIS measurements collected at the start of each sequential discharge showed gradual increases in both ohmic resistance and charge-transfer resistance as the discharge number increased, indicating progressive internal degradation within the cell (**Figure S9**).

To further identify the origin of this voltage decay, we performed cathode recovery experiments after three continuous discharges with 1,500 μm Al anodes. Rinsing the air cathode with deionized water and drying it at 60 °C partially restored the discharge voltage to 1.21 ± 0.09 V, while replacing the used cathode with a fresh cathode recovered the voltage to 1.35 ± 0.06 V, close to the initial value of 1.39 ± 0.07 V (**Figure S10**). These recovery results indicate that the voltage decay is dominated by cathode-side degradation, particularly reversible flooding or surface fouling, rather than irreversible failure of the reusable cell hardware. To further examine cathode degradation, we compared pristine and post-discharge cathodes after long-duration operation. The pristine cathode was highly hydrophobic, with a 1 μL water droplet contact angle of 141.9°. In contrast, the post-discharge cathode became substantially more wettable, with contact angles of 84.2°, 54.7°, and 64.4° measured at three different locations after discharging three 500 μm Al anodes (**Figure S11A**). This loss of hydrophobicity supports cathode flooding as a key contributor to the observed voltage decay.[50,51] SEM images showed no obvious morphological damage to the cathode surface (**Figure S11B**), and XRD measurements showed that the crystalline Pt catalyst peaks were retained in both pristine and post-discharge cathodes, with no obvious new crystalline phase detected (**Figure S11C**). These results suggest that the cathode degradation is primarily associated with wettability change and flooding, rather than structural damage or loss of the crystalline Pt catalyst.

These results support the robustness of the mechanical recharging concept while identifying cathode wetting/flooding as the primary current limitation during extended thick-anode operation. The ability to achieve hundreds of ampere-hours of cumulative capacity through simple anode replacement—without needing to replace the hydrogel or recondition the system—confirms that our hydrogel protection strategy is effective for long-term operation. The strong correlation between discharge energy and anode thickness also provides a practical knob for system-level optimization across applications.

Energy density evolution and projection

To quantify the practical energy density of this mechanically rechargeable system, we define an Al–air battery system that includes the core battery hardware along with its 'fuel': a supply of fresh anodes and electrolyte for microdosing. A key advantage of this system is its evolving energy density, a trend visually captured in **Figure 6A**. The figure plots the cumulative energy delivered as a function of the cumulative carried mass, forming a series of step functions. Each step on the plot corresponds to a single discharge process, where the step's width represents the mass of the added fuel and its height represents

the energy delivered during that discharge. This evolution occurs because each discharge reuses the same fixed hardware mass (~77 g). Consequently, this large initial mass is amortized over a growing cumulative energy output. The system-level energy density at any point is represented by the slope of a line from the origin to that point on the curve; this slope steepens with each anode swap. The system reaches a peak energy density that balances the benefit of amortizing fixed hardware mass against accumulating degradation from mechanisms like cathode flooding and hydrogel fouling.

This effect is demonstrated in **Figure 6A**. For 250 μm anodes (**Table S1**), the system-level energy density increased from an initial 145.1 Wh kg^{-1} to a final value of 435.0 Wh kg^{-1} after ten discharges. The 500 μm anodes (**Table S2**) exhibited a more rapid increase, rising from 232.5 Wh kg^{-1} and peaking at 495.8 Wh kg^{-1} on the eighth discharge before slightly declining to 491.6 Wh kg^{-1} on the tenth. The 1,500 μm anodes (**Table S3**) showed the fastest initial rise, increasing from 465.9 Wh kg^{-1} to 550.5 Wh kg^{-1} over just three discharges. The use of thicker anodes improves the system's energy density more quickly by increasing the mass fraction of the active material in the battery system.

In addition to gravimetric energy density, the mechanically rechargeable architecture produces a similar stepwise evolution in system-level volumetric energy density. Because the core hardware is reused across sequential discharges, the fixed system volume is amortized as additional Al anodes and microdosing electrolyte are consumed. For cells using 1.5 mm thick Al anodes, the system-level volumetric energy density increased from 481 Wh L^{-1} after the first discharge to 656 Wh L^{-1} after three discharges (**Table S4**). This trend mirrors the gravimetric energy-density evolution, although the absolute volumetric energy density is limited by the present prototype design. In particular, the 3D-printed compliant enclosure was intentionally oversized to accommodate anode pouch's expansion and maintain stack pressure, and the ~5mm-thick hydrogel electrolyte contributed a substantial volume. Moreover, we conservatively estimated the core hardware volume using an external bounding box of 92.5 × 82.5 × 15 mm, even though the actual occupied volume of the core hardware was only 49% of this bounding-box volume. These values are therefore best interpreted as prototype-level volumetric performance rather than an optimized packaging limit. Future reductions in casing volume, thinner hydrogel electrolytes, and more compact architectures should further improve the volumetric energy density while retaining the reusable-hardware advantage.

Beyond this baseline, the system's architecture offers unique potential in scenarios where environmental resources can be utilized. The system-level energy density is governed by the total carried mass (hardware plus fuel). If key fuel components are acquired in the environment, the carried mass shrinks and the projected energy density rises dramatically. For example, our system with 1,500 μm anodes achieves 550.5 Wh kg^{-1} after three discharges (**Figure 6B**). If the consumed water were sourced from the environment (e.g., atmospheric harvesting or from a water source on a construction site) instead of carried, the projected energy density would increase to ~970 Wh kg^{-1}. In a more extreme idealization, where both water and aluminum (e.g., scavenged metal scrap or strategically placed Al vending machines) are supplied externally, the projected energy density could exceed 1,570 Wh kg^{-1}.[36] While these projections provide a theoretical upper bound, they highlight a unique advantage of mechanically rechargeable Al–air systems: the potential to far surpass the energy density of conventional batteries by leveraging off-board resources. These resources can be native to the environment or planted in advance to dramatically increase the endurance of robotic or vehicle systems.

Power-density characterization

Power density provides a complementary metric to energy density because it defines the load range over which the battery can operate. Most discharge experiments in this work were performed at 10 mA cm^{-2}, corresponding to 600 mA total current and an areal power density of ~14 mW cm^{-2}. To evaluate sustained power delivery under different loads, we performed a stepwise galvanostatic discharge test using a 500 μm thick Al anode, in which the current density was increased from 1.67 to 16.7 mA cm^{-2}, corresponding to 100 to 1000 mA total current, in 1 h increments (**Figure S12 and Table S5**). At the highest tested current density of 16.7 mA cm^{-2}, the cell sustained an areal power density of ~20 mW cm^{-2}.

Normalized by the initial cell mass and bounding-box volume, including the core hardware and installed Al anode, this corresponds to system-level specific and volumetric power densities of 14.2 W kg^{-1} and 10.8 W L^{-1}, respectively. We also measured the short-timescale peak power capability using linear sweep voltammetry (LSV) in **Figure 7A**. The peak areal power density of ~77 mW cm^{-2} corresponds to system-level specific and volumetric power densities of 53.5 W kg^{-1} and 40.5 W L^{-1}, respectively, using the same normalization basis. Together, the stepwise galvanostatic and LSV measurements define the sustained and instantaneous power limits of the present mechanically rechargeable Al–air architecture.

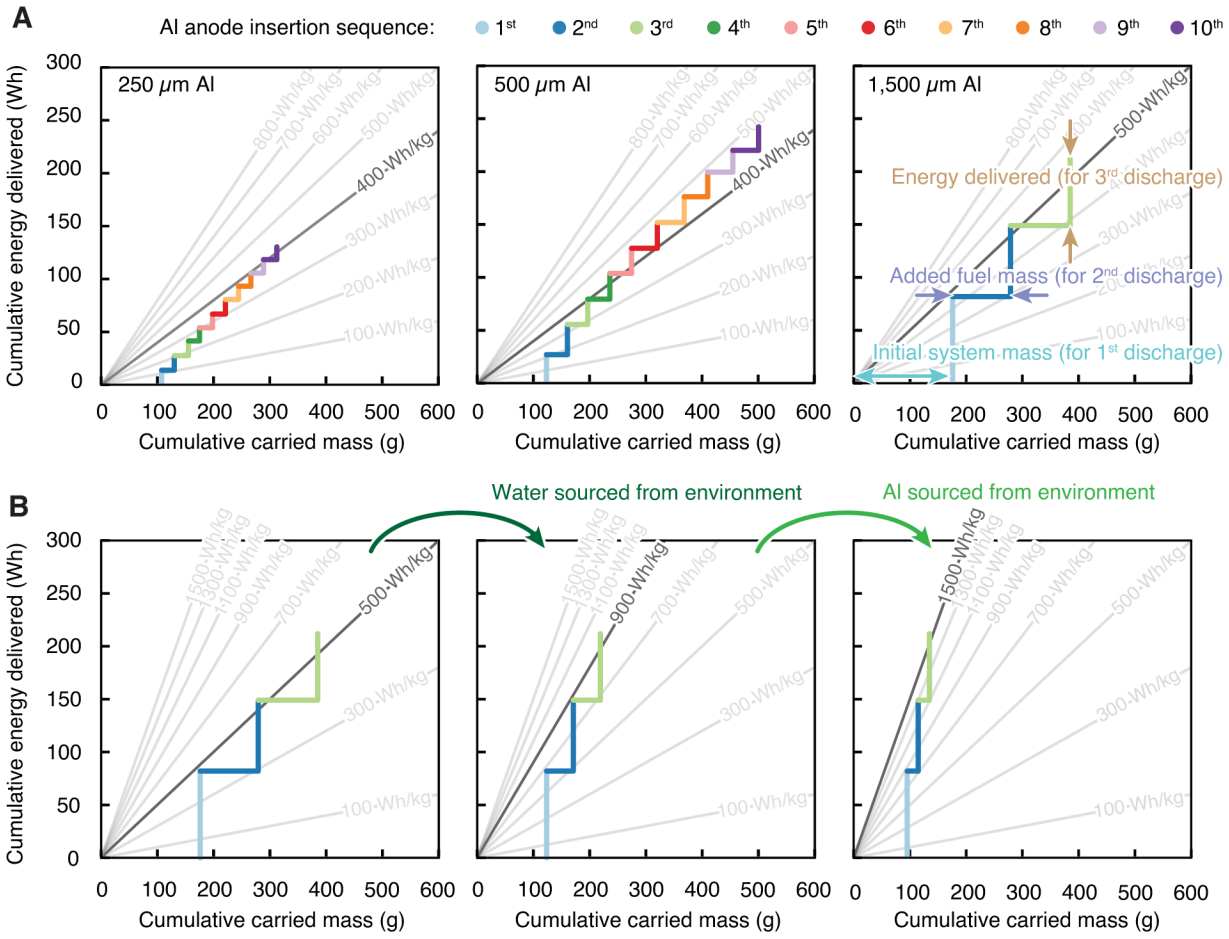


Figure 6. System-level energy density: evolution and projections.
(A) Cumulative energy delivered as a function of cumulative carried system mass for Al–air batteries using 250 μm, 500 μm, and 1,500 μm anodes. The slope of the line from the origin to any point represents the evolving system-level energy density. (B) Projected system-level energy density under idealized conditions with in-situ water harvesting and Al sourcing.

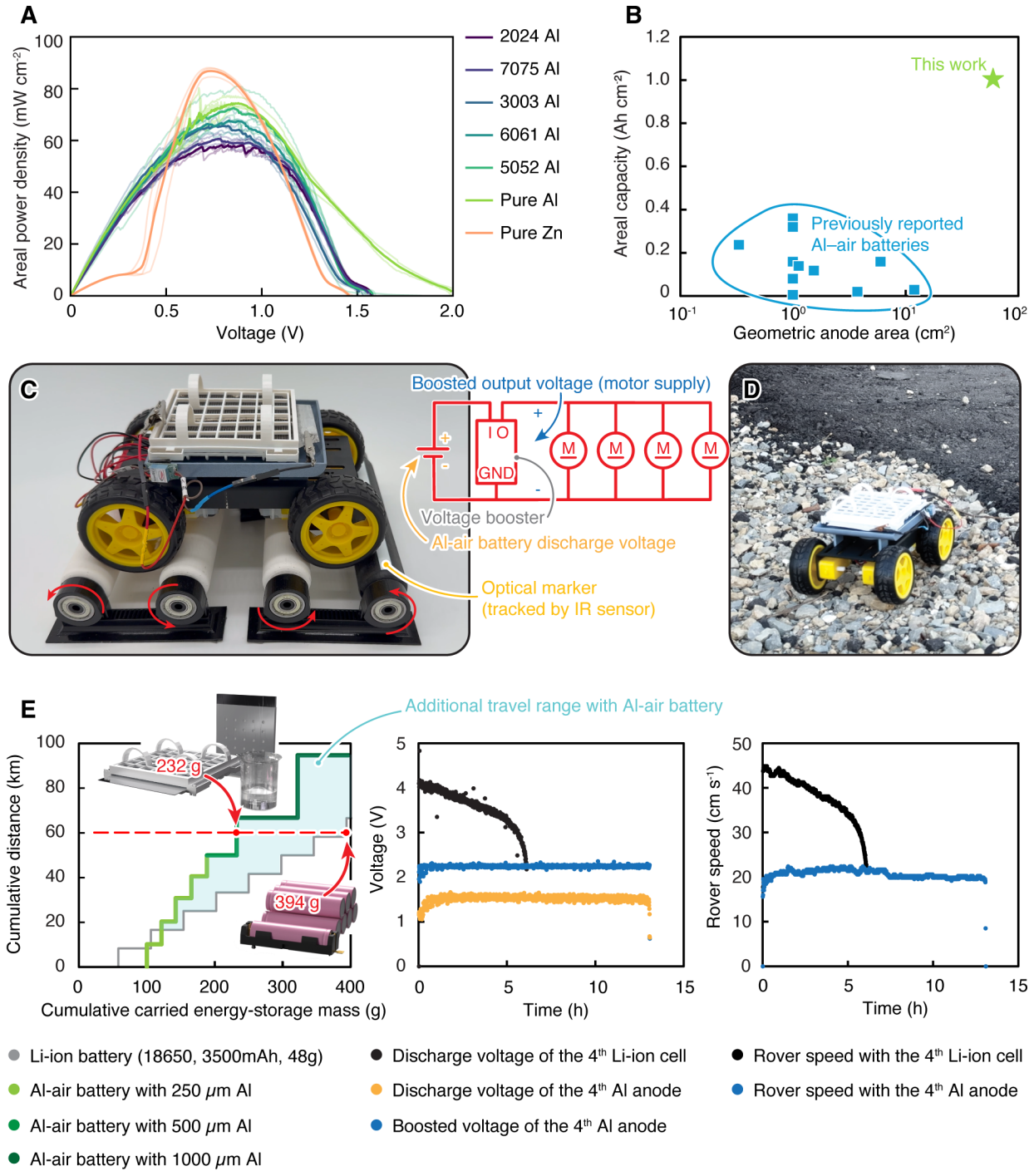


Figure 7. Benchmarking and application in a mobile robot.
(A) Areal power density profiles of mechanically rechargeable metal–air cells with varying anode materials. Thin lines show individual LSV repeats, and thick lines show the mean response. (B) Benchmarking of this work against previously reported Al–air batteries in terms of areal capacity and geometric anode area (detailed data in **Table S6**). (C) The Al–air battery system powering the rover on a dynamometer for endurance testing. (D) The rover operating on outdoor terrain. (E) Performance comparison against a range-matched Li-ion 18650-cell benchmark, comparing cumulative carried energy-storage mass vs. travel distance (left), voltage stability over time (middle), and resulting rover speed (right). Travel distance was calculated as the product of wheel circumference and the total number of wheel rotations recorded.

Application and benchmarking

To simulate a long-range, off-grid mobility application where carried mass is the primary constraint, we benchmarked the system's performance on a robotic rover platform. The custom-built, all-wheel-drive rover was powered by either our Al–air system (coupled with a DC–DC boost converter to regulate voltage at 2.2 V) or a commercial Samsung 18650 Li-ion battery used as the range-matched benchmark. The rover's endurance and speed were quantified on a simplified dynamometer consisting of four rollers, where number of rotations were tracked by an infrared (IR) sensor detecting a high-contrast optical marker on one of the rollers (**Figure 7C, Supplementary Video S3**), and its real-world mobility was further demonstrated in outdoor trials on both paved concrete and gravel (**Figure 7D, Supplementary Video S4**). For robotic missions where extending operational range requires carrying additional energy-storage mass, the Al–air system's evolving energy density provides a significant advantage. **Figure 7E** plots cumulative travel distance versus cumulative carried energy-storage mass for both technologies. For the Al–air system, this mass includes the reusable cell hardware, hydrogel electrolyte, air cathode, manifold, cumulative Al anodes, and all microdosing electrolyte consumed during the mission. For the Li-ion benchmark, this mass includes one lightweight plastic cell holder and all the Samsung 30Q 18650 cells required to achieve the same range. Under this range-matched comparison, the Al–air system achieved a 60 km range with 232 g of carried energy-storage mass, whereas the Li-ion benchmark required 394 g, corresponding to a 41% reduction.

The operational behavior of the rover reflects the distinct discharge characteristics of each power source, as shown in a representative 4th-discharge comparison (**Figure 7E**). The Li-ion battery exhibits a characteristic monotonic voltage decay, dropping from 4.1 V to its 2.8 V cutoff over 6 hours, causing the rover's speed to steadily decrease. In contrast, the Al–air system maintains a stable raw discharge voltage (~1.57 V), which the boost converter regulates to a constant 2.25 V output, resulting in consistent rover speed over 13 hours of operation.

Two system-level factors influence this comparison. First, the Al–air system's lower operating voltage (2.25 V) drives the rover motors more efficiently than the Li-ion's higher voltage range (3.6–4.2 V), yielding a 10–15% improvement in travel efficiency (km Wh^{-1}) as shown in **Figure S13**. Second, the Al–air system requires a DC–DC boost converter with a 70–80% efficiency,[52] introducing energy losses not present in the direct Li-ion configuration. Despite this conversion penalty, the Al–air system's superior energy density enables the 41% mass reduction for equivalent range—a critical advantage for mass-constrained applications. This combination of stable power delivery and reduced carried mass establishes the mechanically rechargeable Al–air battery as a compelling energy solution for long-endurance robotic applications in remote, off-grid environments.

Although the measured system-level power density is modest compared with high-power rechargeable batteries, the sustained output was sufficient to drive four electric motors through a DC–DC boost converter in the rover demonstration, confirming the practical utility of the present design for low-to-moderate-power, long-endurance robotic operation.

To assess whether the mechanically rechargeable architecture can accommodate different metallic fuels, we performed LSV screening with pure Al (99.99%), pure Zn (99.99%), and five common commercial Al alloys under the same 6 M KOH-based electrolyte condition used throughout this work (**Figure 7A**). These measurements characterize the short-timescale response and peak-power capability of each metal within the same platform. Pure Zn produced the highest peak areal power density (~88 mW cm^{-2}), followed by pure Al (~77 mW cm^{-2}), while the tested commercial Al alloys also remained electrochemically active and delivered peak areal power densities of 61–73 mW cm^{-2}. Together with prior studies showing that alkaline Al–air systems can operate with a range of Al alloys and Zn anodes,[53-55] these results indicate that the present architecture is not restricted to a single high-purity Al fuel source.

DISCUSSION

We demonstrate that mechanically rechargeable Al–air systems can operate at a 100-Wh scale when their long-standing interfacial and mechanical failure modes are addressed as a coupled system rather than as isolated chemistry problems. By integrating localized precipitate confinement, controlled interfacial hydration, and mechanically enforced contact with hydrogen venting, our architecture enables uniform utilization of thick Al anodes (up to 1.5 mm) over multi-day operation. The resulting areal capacity of 1.0 Ah cm^{-2} at 82% Al utilization represents a step-change relative to prior Al–air systems (**Figure 7B**), particularly given that it is achieved on 60 cm^2 electrodes rather than on cm-scale laboratory cells.[29,36,56-63] This distinction is not only quantitative but also system-level: whereas many prior approaches improve individual materials or components, such as the anode, electrolyte, or air cathode, this work addresses the coupled device-level requirements needed for repeated operation with reusable cell hardware. These results show that the practical limits of Al–air performance are governed not only by intrinsic electrochemical kinetics, but also by device-level transport, discharge-product management, hydration, gas removal, and interfacial mechanics.

More broadly, this work establishes a practical pathway for operating Al–air in a fuel-cell-like mode, where continuous power delivery is achieved through physical replenishment of aluminum while retaining the hydrogel electrolyte, air cathode, and enclosure. As a result, the fixed mass and volume of the discharge hardware are amortized over successive anode replacements, allowing the effective system-level energy density to increase with use and reach 550 Wh kg^{-1} after three cycles. This behavior is fundamentally different from rechargeable batteries, whose gravimetric energy density is fixed by materials chemistry and packaging. The ability to decouple energy storage (the metal) from power conversion (the discharge hardware) is the central operational advantage of mechanically rechargeable metal–air systems.

Conceptual advances

The central advance of this work is a physics-based architecture for operating a metal–air cell with a growing, insoluble discharge product. In thick-anode Al–air cells, the active interface is a confined multiphase region in which $Al(OH)_3$ precipitation, water consumption, hydrogen generation, volume expansion, and interfacial contact evolve together. Treating these processes independently leads to local blockage, dehydration, gas trapping, and loss of the reusable cell function. Our results show that stable repeated operation requires coordinated control of this coupled chemo-mechanical interface. First, the porous anode pouch confines the mechanically cohesive $Al(OH)_3$ slurry near the anode, preserving the hydrogel and allowing spent product to be removed with the fuel. Second, electrolyte microdosing maintains the $Al(OH)_3$ layer as a hydrated, ionically conductive transport medium rather than allowing it to become a dry passivating barrier. Third, the compliant enclosure and perforated anode manage product swelling, hydrogen removal, and contact pressure as mechanically coupled processes. Together, these principles convert mechanical fuel replacement from a simple refueling concept into a repeatable operating mode with reusable hardware and provide design rules relevant to other metal–air systems, including Zn–air and Fe–air, where discharge products also form at the anode.

Although demonstrated here for Al–air chemistry, the underlying design principles may be relevant to other metal–air systems in which discharge byproducts accumulate, swell, foul interfaces, or disrupt transport. In this broader context, localized product confinement, interfacial hydration control, compliant pressure regulation, gas-management pathways, and hardware-reuse energy accounting provide a general framework for designing mechanically rechargeable metal–air power systems beyond material-level optimization alone.

System-level cost and infrastructure relevance

The practical value of mechanical rechargeability emerges at the system and supply-chain level. Aluminum is non-flammable, easy to handle, and inexpensive to ship, with transportation costs on the order of ~$20 per MWh per 1,000 miles, orders of magnitude lower than Li-ion systems, which require hazardous-material handling and cannot be shipped fully charged in air and many ground applications, and substantially lower than compressed hydrogen. Critically, aluminum is already electrochemically recharged

at trillion-watt-hour scale through the Hall–Héroult smelting process[64], allowing energy to be stored upstream in metallic form and transported as a stable commodity. Zn offers a complementary pathway in which the metal can be electrochemically recharged locally with high round-trip efficiency, not requiring the large infrastructure of Al, enabling substantially lower fuel costs at the tradeoff of reduced energy density. In many real deployments (remote construction, mining, disaster response, and early-stage data center commissioning) the dominant operational cost is not the electrochemical device but the logistics of transporting energy to the point of use. Mechanically rechargeable metal–air systems fit directly into these supply chains by decoupling bulk energy logistics from on-site power conversion.

Why this matters beyond robotics

Although we demonstrate the system on a mobile rover, the underlying constraints are shared by many high-duty-cycle, off-grid, or infrastructure-limited technologies. These include remote mining and excavation equipment, military platforms operating independently of the grid, temporary data centers built ahead of electrical substations, and rapid-deploy power systems for disaster relief. All of these applications require portable, high-energy, safe fuel that can be replenished quickly, not batteries that must sit idle for hours to recharge. By using Al as a transportable energy carrier and decoupling fuel from discharge hardware, mechanically rechargeable Al–air systems address this gap in a way that conventional rechargeable chemistries cannot.

Limitations and future work

Despite the demonstrated performance, several practical limitations remain. Over long operation, the air cathode gradually floods, increasing internal resistance and reducing voltage. Hydrogel electrolytes help to reduce flooding due to their high water affinity,[65,66] but improved water management at the hydrogel–cathode interface or methods to quickly regenerate the air-cathode will be required for higher cycle counts. The porous anode pouch effectively captures $Al(OH)_3$, but its filtration efficiency ultimately limits year-long operation as small precipitates diffuse to the hydrogel interface. Although replacing the hydrogel is low cost (~$0.70 per unit for the size and formulation used in this work, with significant cost reductions expected at industrial scale), future pouch materials with engineered pore structure or graded wettability could further increase the longevity of hydrogel interfaces without compromising on ionic conductivity. Finally, although the PAAm hydrogel maintained its mechanical integrity and remained functional during the demonstrated multi-day discharge tests, its durability over substantially longer operating periods, such as weeks to months of repeated mechanical recharging, remains to be established. Double network hydrogels can increase toughness without losing the conductivity and hydration benefits.[26,67] Addressing these issues will be essential for scaling mechanically rechargeable Al–air systems to higher power, larger area, and fully autonomous refueling operation.

A second limitation is that electrolyte microdosing was implemented using a fixed 30 min interval in this study. Although the delivered electrolyte rate was systematically varied and 60 $\mu L\ cm^{-2}\ h^{-1}$ was selected because it maintained ionic pathways through the $Al(OH)_3$ layer while minimizing hydrogel degradation and electrolyte waste, the temporal dosing strategy itself was not dynamically optimized. Future systems could use adaptive microdosing protocols that vary injection frequency and volume in response to cell voltage, impedance, humidity, electrolyte inventory, or discharge current. Such feedback-controlled dosing could further improve water management, reduce electrolyte waste, and support autonomous long-duration operation.

The present prototype was also optimized primarily for gravimetric energy density and mechanical rechargeability, rather than compact volumetric packaging. As a result, the volumetric energy and power densities are far lower than their optimal values. Future designs should translate the packaging functions into more compact architectures through reduced enclosure dead volume, thinner hydrogel electrolytes, and integrated stack packaging.

Power density also remains another key area for future optimization. The Al–air battery's power output is limited by ORR kinetics and oxygen transport, as well as by ionic transport through the hydrogel

electrolyte and evolving $Al(OH)_3$ precipitate. System-level specific and volumetric power densities are further reduced by inactive mass and volume from the reusable enclosure and hydrogel electrolyte, which are required for swelling accommodation, stack pressure, hydration, and mechanical rechargeability. Future improvements could therefore target both cell-level power output and system-level packaging: accelerating cathodic ORR kinetics, improving oxygen transport and cathode water management, reducing ionic/contact resistance, increasing the effective Al surface area through structured anodes, and reducing inactive mass and volume through thinner hydrogel electrolytes, stronger lightweight casing materials, and more compact stack architectures. For applications with transient high-power demands, the Al–air module could also be integrated with power-buffering components such as supercapacitors or Li-ion batteries.

Taken together, these limitations define clear directions for translating mechanically rechargeable Al–air systems from laboratory prototypes to practical long-duration power sources. The present results show that Al–air can be engineered into a functional, field-serviceable system when its mechanical, interfacial, and transport limitations are addressed coherently. By enabling thick-anode utilization, rapid mechanical refueling, and fuel-cell-like continuous operation, this architecture establishes a new operational regime for metal–air systems and a practical path toward aluminum-based power for long-endurance, off-grid technologies.

METHODS

Fabrication of the hydrogel electrolyte

PAAm hydrogels were prepared by free-radical polymerization. First, 20 g of acrylamide monomer (Sigma-Aldrich, A8887) was dissolved in 80 g of deionized water and stirred for 60 min. To this solution, 1.5 mL of 20 mg mL^{-1} N,N'-methylenebis(acrylamide) (Sigma-Aldrich, 146072) as a crosslinker and 250 mg of ammonium persulfate (Sigma-Aldrich, 248614) as an initiator were added and stirred for 15 min. The mixture was degassed for 15 min, followed by the addition of 30 µL tetramethylethylenediamine (TEMED, Sigma-Aldrich, T7024) to accelerate polymerization. The solution was then poured into molds and allowed to polymerize into cross-linked PAAm hydrogels. Formed hydrogels were dried in an oven at 60 °C for 6 h, then soaked in 6 M KOH (Sigma-Aldrich, 221473) containing 0.05 M K_2SnO_3 (Sigma-Aldrich, 462799) for at least 48 h to load electrolyte. Finally, the hydrogels were cut into the desired shape for testing and assembly.

Anode preparation

A variety of metallic anodes were tested. High-purity Al (99.99%) sheets were used for primary tests in three thicknesses: 250 µm (Thermo Fisher Scientific, 040761.HP), 500 µm (Thermo Fisher Scientific, 040531.HP), and 1,500 µm (Thermo Fisher Scientific, 044491.HP). These configurations resulted in total initial battery masses of approximately 81 g, 86 g, and 105 g, respectively. For benchmarking (**Figure 7A**), additional anodes were used, including a 99.99% Zn sheet (Thermo Fisher Scientific, 011912.HG) and six commercial Al alloys: 6061 (McMaster-Carr, 1651T1), 5052 (McMaster-Carr, 8199K101), 7075 (McMaster-Carr, 8885K11), 2024 (McMaster-Carr, 88835K12), 3003 (McMaster-Carr, 8973K351), and 1100 (McMaster-Carr, 2471T93). All metal sheets were first cut to the desired dimensions using a precision shear. To facilitate hydrogen gas release, a perforation pattern (30 circular holes, 0.75 mm diameter, 7 mm spacing) was introduced using a handheld drill. After drilling, the anodes were rinsed with ethanol. Finally, each prepared anode was inserted into a commercial porous polymer pouch (Amazon, B0BN1KHYSS) before being assembled into the battery.

Fabrication of Al–air battery

The battery enclosures were fabricated by 3D printing (Stratasys, Objet30 Pro). Four pairs of neodymium magnets (Amazon, B08L3FVFFZ) were positioned at the corners to align the enclosure during assembly. The internal stack, arranged from cathode to anode, consisted of an electroformed nickel micro-mesh current collector (Precision Eforming, MN69), a 60 cm^2 commercial gas diffusion electrode (Fuel Cell Store, W1S1011) composed of 4.0 mg cm^{-2} platinum on carbon cloth (serving as the air cathode), the

prepared hydrogel electrolyte, and the prepared anode pouch. The air cathode was bonded to the nickel mesh current collector using a silver conductive epoxy (MG Chemicals, 8331D).

Standardized operational protocol for mechanical recharging

After each discharge, the cell was disconnected from the external circuit and electrolyte microdosing was paused. For routine mechanical recharging, the spent anode pouch, containing the consumed Al anode and accumulated $Al(OH)_3$ slurry, was removed as a single replaceable unit through the front access slot of the spring-loaded cassette. A new anode pouch with fresh Al inside was then inserted into the cassette through the same access slot, and electrolyte microdosing was resumed to start the next discharge. For cases where the spent anode pouch underwent substantial swelling and became difficult to remove through the access slot, such as after discharge of 1,500 μm thick Al anodes, the cassette was manually opened to remove the spent pouch. After removal, the cassette was closed again, with the magnets at the four corners of the top and bottom enclosures providing automatic alignment. A fresh anode pouch was then inserted into the cell, and discharge was restarted.

Electrolyte microdosing

Electrolyte microdosing can be performed either manually or automatically. For manual dosing, a syringe fitted with an 18-gauge blunt-tip needle was aligned with the inlet of the electrolyte distribution manifold and the desired volume was injected. For testing consistency during electrochemical characterization, automated microdosing was applied, using a compact 6.5 g micropump (Amazon, B074T95GGX) that is triggered every 30 min to inject 0.9 mL (30 μL cm^{-2} h^{-1}), 1.8 mL (60 μL cm^{-2} h^{-1}), and 4.8 mL (160 μL cm^{-2} h^{-1}) into the microdosing manifold. The microdosing solution was identical to the hydrogel soak electrolyte. Unless otherwise stated, 60 μL cm^{-2} h^{-1} was used for all experiments. This 60 μL cm^{-2} h^{-1} microdosing rate is substantially higher than the measured passive evaporation rate (2 μL cm^{-2} h^{-1}) under ambient conditions, indicating that the dosing strategy provides sufficient water input to compensate hydrogel evaporation while supporting electrochemical water consumption and $Al(OH)_3$ slurry hydration. The mass of the auxiliary micropump for this automated setup was excluded from system-level energy density calculations. This calculation boundary is set to define the performance of the core energy module (fixed hardware ~77g plus fuel), as the pump is considered an auxiliary, application-specific component for platform integration, similar to the voltage booster (3.5 g).

Electrochemical characterization

All electrochemical measurements were performed using a multichannel potentiostat (BioLogic Science Instruments, VMP3). Galvanostatic discharge tests were conducted at a constant current of 600 mA, corresponding to a current density of 10 mA cm^{-2}. Electrochemical impedance spectroscopy was carried out with a sinusoidal perturbation of 10 mV amplitude over the frequency range of interest. For benchmarking of different metallic anodes, LSV was performed using the same instrument, scanning from the open-circuit voltage to 0 V at a rate of 10 mV s^{-1}. All experiments were performed at 24°C and 40% relative humidity.

Experimental setup for rover benchmarking

The rover experiments were performed using a custom-built all-wheel-drive platform powered directly by the Al–air battery system. An Arduino Uno microcontroller was used for data acquisition, equipped with an IR sensor module positioned to detect a high-contrast optical marker on one roller of a dynamometer. The IR signal was connected to a digital interrupt pin to count wheel rotations, while the supply voltage from the battery was continuously monitored through an analog input channel. To benchmark endurance and stability, the rover was operated continuously until either the Al–air battery or the Li-ion battery was fully discharged, with the logged data used to calculate speed, distance traveled, and voltage stability. The voltage booster used was a 3.5 g commercial model (Dimension Engineering, LVBoost), and the Li-ion battery used for benchmarking was a 48g, 3Ah, 18650 battery (SAMSUNG, 30Q 18650).

Calculations for transportation cost of bulk Al, hydrogen, and Li-ion battery

Normalized transportation costs (USD per MWh per 1,000 miles) were calculated for each energy carrier. For Li-ion batteries, we used the model from Dai et al. estimating a shipping cost of $1.93 per ton-mile based on American Transportation Research Institute (ATRI) freight data.[20,21] Assuming a representative system-level energy density of 200 Wh/kg, this yields a normalized transportation cost of ~$10,000 per MWh per 1,000 miles. For hydrogen fuel compressed at 350 bar, Solomon et al. report a transport cost (truck fuel + truck labor) of approximately €1 per 1 kg per 500 km; based on the energy density of hydrogen (33 kWh/kg), this cost converts to ~$120 per MWh per 1,000 miles.[19,68] In contrast, aluminum is a common, non-hazardous commodity. This analysis adopts the standard ATRI freight trucking rate for a "truckload dry van" of $3.015 per mile per truckload. Assuming a standard truckload capacity of 22 tons and using the theoretical energy density of aluminum (8100 Wh/kg), the resulting transportation cost is approximately ~$20 per MWh per 1,000 miles.[18]

Calculations for anode utilization efficiency

Anode utilization efficiencies were determined by mass balance. The initial and final mass of each anode was recorded to find the total mass consumed. The mass of aluminum consumed by electrochemical oxidation was calculated from the measured discharge capacity using Faraday's law. The difference between the total consumed mass and oxidized mass was attributed to parasitic hydrogen evolution. Utilization efficiency was defined as oxidized mass divided by the initial mass of a 60 cm² anode (active region).

Calculations for water and electrolyte mass balance

The mass balance of water and electrolyte was quantified by comparing measured inputs and outputs, normalized to capacity. Inputs included electrolyte released from the hydrogel (measured by hydrogel mass change) and electrolyte from microdosing (measured by reservoir mass change). Outputs (sinks) were: (1) stoichiometric water consumption from the oxidation reaction, calculated from the discharge capacity; (2) water consumption from parasitic HER, calculated from the HER-attributed mass loss, using the corresponding reaction stoichiometry; and (3) hydration of the $Al(OH)_3$ slurry, quantified by measuring the pouch mass before and after oven-drying. Any remaining discrepancy between inputs and outputs was attributed to evaporation and KOH loss. The mass of K_2SnO_3 was excluded from analysis due to its low concentration.

Calculations for specific capacity, specific energy, and system-level gravimetric energy density

In **Figure 4**, Al-specific capacity (Ah kg^{-1}_{Al}) and Al-specific energy (Wh kg^{-1}_{Al}) were normalized by the mass of the Al anode's electrochemically active region. In **Figure 6** and **Table S1-S3**, system-level gravimetric energy density (Wh kg^{-1}) was determined from the cumulative discharge energy over *n* sequential discharges, normalized by the total carried mass. This system mass includes the fixed hardware (enclosure, hydrogel, cathode, manifold), all n anodes, and the total microdosing electrolyte consumed. In **Table S4**, system-level volumetric energy density (Wh L^{-1}) was determined from the cumulative discharge energy over *n* sequential discharges, normalized by the corresponding total carried volume. This volume includes the fixed core hardware volume, the cumulative volume of all *n* consumed Al anodes, and the total volume of microdosing electrolyte consumed during those discharges. The fixed core hardware volume includes the enclosure, hydrogel electrolyte, air cathode, and microdosing manifold. It was estimated using an external bounding-box volume of 92.5 × 82.5 × 15 mm. Because of the irregular geometry of the enclosure, approximately half of this bounding-box volume is occupied by the core hardware. The four curved spring elements of the top enclosure, with a total volume of approximately 1.84 cm³, were excluded from the bounding-box volume calculation.

Calculations for areal power density, system-level specific power density and volumetric power density

Areal power density (mW cm^{-2}) was calculated from the measured cell voltage and the applied current density, using an active electrode area of 60 cm². For the stepwise galvanostatic discharge test in **Figure S12** and **Table S5**, the sustained areal power density at each current step was calculated by multiplying the average voltage during that step by the corresponding current density. Current densities from 1.67 to 16.7 mA cm^{-2} corresponded to total currents from 100 to 1000 mA for the 60 cm² reaction

area. System-level specific power density (W kg^{-1}) was calculated by normalizing the total cell power by the initial cell mass, which includes the fixed core hardware and the installed Al anode. System-level volumetric power density (W L^{-1}) was calculated by normalizing the total cell power by the initial bounding-box volume of the core hardware with the installed Al anode. For the LSV measurements, instantaneous power was calculated from the measured voltage and current, and the peak power density was determined from the maximum value of the resulting power.

RESOURCE AVAILABILITY

Lead contact

Requests for further information and resources should be directed to and will be fulfilled by the lead contact, James Pikul (jpikul@wisc.edu).

Materials availability

This study did not generate new unique reagents.

ACKNOWLEDGMENTS

This research was partially funded by the Gordon and Betty Moore Foundation.

AUTHOR CONTRIBUTIONS

Conceptualization, Y.S. and J.H.P.; methodology, Y.S., E.J., M.R., and J.H.P.; investigation, Y.S., M.R., E.J., J.K., X.C., H.W., and J.H.P.; writing—original draft, Y.S. and J.H.P.; writing—revised draft, Y.S. and J.H.P.; writing—review & editing, Y.S. and J.H.P.; funding acquisition, J.H.P.; resources, J.H.P.; supervision, J.H.P.

DECLARATION OF INTERESTS

Y.S. and J.H.P. have submitted a patent application that covers some of the work presented.

DECLARATION OF GENERATIVE AI AND AI-ASSISTED TECHNOLOGIES IN THE MANUSCRIPT PREPARATION PROCESS

During the preparation of this work the authors used Gemini 3 and ChatGPT to edit and check grammar. After using this tool/service, the authors reviewed and edited the content as needed and take full responsibility for the content of the published article.

SUPPLEMENTAL INFORMATION

Document S1. Supplemental methods, Figures S1–S13, and Tables S1–S6
Video S1: Demonstration of the rapid mechanical recharging process and microdosing
Video S2: Comparison of hydrogen gas management with and without anode perforations and applied stack pressure
Video S3: Demonstration of an Al–air-powered rover on the customized dynamometer
Video S4: Field demonstration of an Al–air-powered rover on outdoor terrain

REFERENCES

1. Spot® - The Agile Mobile Robot. https://bostondynamics.com/products/spot/.
2. 320 Electric Medium Excavator. https://www.cat.com/en_US/by-industry/construction/electric-products.html.
3. Yue, X., Johnson, A.C., Kim, S., Kohlmeyer, R.R., Patra, A., Grzyb, J., Padmanabha, A., Wang, M., Jiang, Z., Sun, P., et al. (2021). A Nearly Packaging-Free Design Paradigm for Light, Powerful, and Energy-Dense Primary Microbatteries. Advanced Materials *33*, 2101760. https://doi.org/10.1002/adma.202101760.
4. Energy and AI. (2025). International Energy Agency. https://www.iea.org/reports/energy-and-ai.
5. Jones, N. (2018). How to stop data centres from gobbling up the world's electricity. Nature *561*, 163-166. https://doi.org/10.1038/d41586-018-06610-y.
6. Janek, J., and Zeier, W.G. (2016). A solid future for battery development. Nature Energy *1*, 16141. https://doi.org/10.1038/nenergy.2016.141.
7. Yao, A., Benson, S.M., and Chueh, W.C. (2025). Critically assessing sodium-ion technology roadmaps and scenarios for techno-economic competitiveness against lithium-ion batteries. Nature Energy *10*, 404-416. https://doi.org/10.1038/s41560-024-01701-9.
8. Xu, L., Tang, S., Cheng, Y., Wang, K., Liang, J., Liu, C., Cao, Y.-C., Wei, F., and Mai, L. (2018). Interfaces in Solid-State Lithium Batteries. Joule *2*, 1991-2015. https://doi.org/10.1016/j.joule.2018.07.009.
9. Li, M., Lu, J., Chen, Z., and Amine, K. (2018). 30 Years of Lithium-Ion Batteries. Advanced Materials *30*, 1800561. https://doi.org/10.1002/adma.201800561.
10. Kazyak, E., Chen, K.-H., Chen, Y., Cho, T.H., and Dasgupta, N.P. (2022). Enabling 4C Fast Charging of Lithium-Ion Batteries by Coating Graphite with a Solid-State Electrolyte. Advanced Energy Materials *12*, 2102618. https://doi.org/10.1002/aenm.202102618.
11. Delmas, C. (2018). Sodium and Sodium-Ion Batteries: 50 Years of Research. Advanced Energy Materials *8*, 1703137. https://doi.org/10.1002/aenm.201703137.
12. Jung, D., Cho, Y., Kim, D., Piao, S., Hahn, M., Kim, C.W., and Piao, Y. (2024). Enhancing Lithium-Ion Diffusion Kinetics in a 3D Lithium Metal Host through Surface Modification with Hierarchical Multimetal Oxides. ACS Applied Materials & Interfaces *16*, 28319-28332. https://doi.org/10.1021/acsami.3c18124.
13. Sugano, K., Mair, S., Ganti-Agrawal, S., Friesen, A.S., Raman, K., Woodford, W.H., Sripad, S., Viswanathan, V., and Chiang, Y.-M. (2025). Sodium-air fuel cell for high energy density and low-cost electric power. Joule *9*. https://doi.org/10.1016/j.joule.2025.101962.
14. Lee, J.-S., Tai Kim, S., Cao, R., Choi, N.-S., Liu, M., Lee, K.T., and Cho, J. (2011). Metal–Air Batteries with High Energy Density: Li–Air versus Zn–Air. Advanced Energy Materials *1*, 34-50. https://doi.org/10.1002/aenm.201000010.
15. Rani, B., Yadav, J.K., Saini, P., Pandey, A.P., and Dixit, A. (2024). Aluminum–air batteries: current advances and promises with future directions. RSC Advances *14*, 17628-17663. https://doi.org/10.1039/D4RA02219J.
16. Ryu, J., Park, M., and Cho, J. (2019). Advanced Technologies for High-Energy Aluminum–Air Batteries. Advanced Materials *31*, 1804784. https://doi.org/10.1002/adma.201804784.
17. Faegh, E., Ng, B., Hayman, D., and Mustain, W.E. (2021). Practical assessment of the performance of aluminium battery technologies. Nature Energy *6*, 21-29. https://doi.org/10.1038/s41560-020-00728-y.
18. Leslie, A., and Murray, D. (2025). An Analysis of the Operational Costs of Trucking: 2025 Update. Technical report American Transportation Research Institute. July 2025.
19. Solomon, M.D., Heineken, W., Scheffler, M., and Birth-Reichert, T. (2024). Cost Optimization of Compressed Hydrogen Gas Transport via Trucks and Pipelines. Energy Technology *12*, 2300785. https://doi.org/10.1002/ente.202300785.
20. Slattery, M., Dunn, J., and Kendall, A. (2021). Transportation of electric vehicle lithium-ion batteries at end-of-life: A literature review. Resources, Conservation and Recycling *174*, 105755. https://doi.org/10.1016/j.resconrec.2021.105755.
21. Dai, Q., Spangenberger, J., Ahmed, S., Gaines, L., Kelly, J., and Wang, M. (2019). EverBatt: A Closed-loop Battery Recycling Cost and Environmental Impacts Model. Office of Scientific and Technical Information (OSTI). https://dx.doi.org/10.2172/1530874.
22. Ng, K.L., Amrithraj, B., and Azimi, G. (2022). Nonaqueous rechargeable aluminum batteries. Joule *6*, 134-170. https://doi.org/10.1016/j.joule.2021.12.003.
23. Wang, H.-F., and Xu, Q. (2019). Materials Design for Rechargeable Metal-Air Batteries. Matter *1*, 565-595. https://doi.org/10.1016/j.matt.2019.05.008.
24. Zhu, Y., Hua, Z., Lu, Y., Wang, Z., Tian, Z., and Peng, K. (2023). Effect Factors on the Performances of Commercial Al Alloy as Anode for Al-Air Batteries. Energy & Fuels *37*, 11367-11375. 10.1021/acs.energyfuels.3c01504.
25. Zhao, R., He, P., Yu, F., Yang, J., Sun, Z., and Hu, W. (2023). Performance improvement for aluminum-air battery by using alloying anodes prepared from commercially pure aluminum. Journal of Energy Storage *73*, 108985. https://doi.org/10.1016/j.est.2023.108985.

26. Ren, M., Shi, Y., Xiao, L., Sun, A., Johnston, E., Mallouk, T.E., Allen, M., and Pikul, J.H. (2024). Biodegradable hydrogels with tunable cross-linking structures regulate Al oxidation in Al–air batteries. MRS Communications *14*, 1045-1053. https://doi.org/10.1557/s43579-024-00598-5.
27. Lv, C., Zhang, Y., Ma, J., Zhu, Y., Huang, D., Li, Y., Wang, H., and Tang, Y. (2022). Regulating solvation and interface chemistry to inhibit corrosion of the aluminum anode in aluminum–air batteries. Journal of Materials Chemistry A *10*, 9506-9514. https://doi.org/10.1039/D2TA01064J.
28. Xue, Y., Miao, H., Sun, S., Wang, Q., Li, S., and Liu, Z. (2017). (La1−xSrx)0.98MnO3 perovskite with A-site deficiencies toward oxygen reduction reaction in aluminum-air batteries. Journal of Power Sources *342*, 192-201. https://doi.org/10.1016/j.jpowsour.2016.12.065.
29. Hopkins, B.J., Shao-Horn, Y., and Hart, D.P. (2018). Suppressing corrosion in primary aluminum–air batteries via oil displacement. Science *362*, 658-661. https://doi.org/10.1126/science.aat9149.
30. Park, M., Ryu, J., Wang, W., and Cho, J. (2016). Material design and engineering of next-generation flow-battery technologies. Nature Reviews Materials *2*, 16080. https://doi.org/10.1038/natrevmats.2016.80.
31. Sheerin, G.T. (2018) Air metal battery having a rotating anode and a cathode assembly. United States patent US10978758B2.
32. Blurton, K.F., and Sammells, A.F. (1979). Metal/air batteries: Their status and potential — a review. Journal of Power Sources *4*, 263-279. https://doi.org/10.1016/0378-7753(79)80001-4.
33. Shi, Y., and Pikul, J.H. (2025). Achieving animal endurance in robots through advanced energy storage. Science Robotics *10*, eadr6125. https://doi.org/10.1126/scirobotics.adr6125.
34. Liang, Z., He, J., Hu, C., Pu, X., Khani, H., Dai, L., Fan, D., Manthiram, A., and Wang, Z.-L. (2023). Next-Generation Energy Harvesting and Storage Technologies for Robots Across All Scales. Advanced Intelligent Systems *5*, 2200045. https://doi.org/10.1002/aisy.202200045.
35. Boudreau, P., Johnson, M., and Bergthorson, J.M. (2024). Techno-economic assessment of aluminum as a clean energy carrier to decarbonize remote industries. Energy Advances *3*, 1919-1931. https://doi.org/10.1039/d4ya00151f.
36. Wang, M., Joshi, U., and Pikul, J.H. (2020). Powering Electronics by Scavenging Energy from External Metals. ACS Energy Letters *5*, 758-765. https://doi.org/10.1021/acsenergylett.9b02661.
37. Wei, Y., Shi, Y., Chen, Y., Xiao, C., and Ding, S. (2021). Development of solid electrolytes in Zn–air and Al–air batteries: from material selection to performance improvement strategies. Journal of Materials Chemistry A *9*, 4415-4453.
38. Abbasi, A., Xu, Y., Khezri, R., Etesami, M., Lin, C., Kheawhom, S., and Lu, Y. (2022). Advances in characteristics improvement of polymeric membranes/separators for zinc-air batteries. Materials Today Sustainability *18*, 100126. https://doi.org/10.1016/j.mtsust.2022.100126.
39. Sun, P., Chen, J., Huang, Y., Tian, J.-H., Li, S., Wang, G., Zhang, Q., Tian, Z., and Zhang, L. (2021). High-Strength agarose gel electrolyte enables long-endurance wearable Al-air batteries with greatly suppressed self-corrosion. Energy Storage Materials *34*, 427-435. https://doi.org/10.1016/j.ensm.2020.10.009.
40. Gaele, M.F., and Di Palma, T.M. (2022). Polymer Electrolytes for Al-Air Batteries: Current State and Future Perspectives. Energy & Fuels *36*, 12875-12895. https://doi.org/10.1021/acs.energyfuels.2c02453.
41. Zhao, S., Xia, D., Li, M., Cheng, D., Wang, K., Meng, Y.S., Chen, Z., and Bae, J. (2021). Self-Healing and Anti-CO2 Hydrogels for Flexible Solid-State Zinc-Air Batteries. ACS Applied Materials & Interfaces *13*, 12033-12041. https://doi.org/10.1021/acsami.1c00012.
42. Parvar, S., Chaparian, E., and Tammisola, O. (2024). General hydrodynamic features of elastoviscoplastic fluid flows through randomised porous media. Theoretical and Computational Fluid Dynamics *38*, 531-544. 10.1007/s00162-024-00705-1.
43. Liu, C., Sun, T., Chen, W., Zhang, H., Huang, P., Yang, L., Yao, Y., Peng, Q., Hu, Y., Meng, Y., et al. Ultra-High Friction and Adhesion in Hydrogel Layer Driven by Wet-to-Dry Transition Dynamics. Advanced Science *n/a*, e07827. https://doi.org/10.1002/advs.202507827.
44. Zhou, Z., Lei, J., and Liu, Z. (2022). Effect of water content on physical adhesion of polyacrylamide hydrogels. Polymer *246*, 124730. https://doi.org/10.1016/j.polymer.2022.124730.
45. Ying, B., Chen, R.Z., Zuo, R., Li, J., and Liu, X. (2021). An Anti-Freezing, Ambient-Stable and Highly Stretchable Ionic Skin with Strong Surface Adhesion for Wearable Sensing and Soft Robotics. Advanced Functional Materials *31*, 2104665. https://doi.org/10.1002/adfm.202104665.
46. Cifrain, M., and Kordesch, K.V. (2004). Advances, aging mechanism and lifetime in AFCs with circulating electrolytes. Journal of Power Sources *127*, 234-242. https://doi.org/10.1016/j.jpowsour.2003.09.019.
47. Gelman, D., Lasman, I., Elfimchev, S., Starosvetsky, D., and Ein-Eli, Y. (2015). Aluminum corrosion mitigation in alkaline electrolytes containing hybrid inorganic/organic inhibitor system for power sources applications. Journal of Power Sources *285*, 100-108. https://doi.org/10.1016/j.jpowsour.2015.03.048.
48. Chu, D., and Savinell, R.F. (1991). Experimental data on aluminum dissolution in KOH electrolytes. Electrochimica Acta *36*, 1631-1638. https://doi.org/10.1016/0013-4686(91)85017-2.
49. Liu, X., Dong, Y., Ma, J., Huang, J., Wang, Z., Cheng, S., Li, X., Xue, J., Zhou, W., and Qian, Z. (2026). Synergistic interface engineering with anionic imidazole and stannate for hydrogen evolution suppression in

aluminum–air batteries. Journal of Power Sources *667*, 239325. https://doi.org/10.1016/j.jpowsour.2026.239325.
50. Yang, Y., Qin, J., Hu, K., Luo, L., Kumar, A., Zhou, D., Zhuang, Z., Li, H., and Sun, X. (2023). Self-flooding behaviors on the fuel cell catalyst surface: an in situ mechanism investigation. Energy & Environmental Science *16*, 491-501.
51. Fathi, H., Raoof, A., and Mansouri, S. (2017). Insights into the role of wettability in cathode catalyst layer of proton exchange membrane fuel cell; pore scale immiscible flow and transport processes. Journal of Power Sources *349*, 57-67.
52. LVBoost. https://www.dimensionengineering.com/products/lvboost.
53. Shi, Y., Ren, M., Sun, A., Johnston, E.D., Allen, M.G., and Pikul, J.H. (2024). Stretchable Metal-Air Batteries Through Sliding Electrodes. Advanced Functional Materials *34*, 2314783. https://doi.org/10.1002/adfm.202314783.
54. Wu, S., Zhang, Q., Ma, J., Sun, D., Tang, Y., and Wang, H. (2020). Interfacial design of Al electrode for efficient aluminum-air batteries: issues and advances. Materials Today Energy *18*, 100499.
55. Jiang, M., Fu, C., Meng, P., Ren, J., Wang, J., Bu, J., Dong, A., Zhang, J., Xiao, W., and Sun, B. (2022). Challenges and strategies of low‐cost aluminum anodes for high‐performance Al‐based batteries. Advanced Materials *34*, 2102026.
56. Gelman, D., Shvartsev, B., and Ein-Eli, Y. (2014). Aluminum–air battery based on an ionic liquid electrolyte. Journal of Materials Chemistry A *2*, 20237-20242. https://doi.org/10.1039/C4TA04721D.
57. Katsoufis, P., Katsaiti, M., Mourelas, C., Andrade, T.S., Dracopoulos, V., Politis, C., Avgouropoulos, G., and Lianos, P. (2020). Study of a Thin Film Aluminum-Air Battery. Energies *13*, 1447. https://doi.org/10.3390/en13061447.
58. Yu, Y., Chen, M., Wang, S., Hill, C., Joshi, P., Kuruganti, T., and Hu, A. (2018). Laser Sintering of Printed Anodes for Al-Air Batteries. Journal of The Electrochemical Society *165*, A584. https://doi.org/10.1149/2.0811803jes.
59. Tan, M.J., Li, B., Chee, P., Ge, X., Liu, Z., Zong, Y., and Loh, X.J. (2018). Acrylamide-derived freestanding polymer gel electrolyte for flexible metal-air batteries. Journal of Power Sources *400*, 566-571. https://doi.org/10.1016/j.jpowsour.2018.08.066.
60. Liu, X., Zhang, P., Xue, J., Zhu, C., Li, X., and Wang, Z. (2021). High energy efficiency of Al-based anodes for Al-air battery by simultaneous addition of Mn and Sb. Chemical Engineering Journal *417*, 128006. https://doi.org/10.1016/j.cej.2020.128006.
61. Rani, B., Yadav, J.K., Saini, P., Pandey, A.P., and Dixit, A. (2024). Impact of aluminum alloy grade as anode on electrochemical performance for Al-Air cell in alkaline electrolyte. Energy Storage *6*, e586. https://doi.org/10.1002/est2.586.
62. Lv, C., Li, Y., Zhu, Y., Zhang, Y., Kuang, J., Zhao, Q., Tang, Y., and Wang, H. (2023). Quasi-Solid-State Aluminum–Air Batteries with Ultra-high Energy Density and Uniform Aluminum Stripping Behavior. Advanced Science *10*, 2304214. https://doi.org/10.1002/advs.202304214.
63. Zhang, Z., Zuo, C., Liu, Z., Yu, Y., Zuo, Y., and Song, Y. (2014). All-solid-state Al–air batteries with polymer alkaline gel electrolyte. Journal of Power Sources *251*, 470-475. https://doi.org/10.1016/j.jpowsour.2013.11.020.
64. Primary Aluminium Smelting Power Consumption. (2024). International Aluminium Institute. https://international-aluminium.org/statistics/primary-aluminium-smelting-power-consumption/.
65. Sankaralingam, R.K., Seshadri, S., Sunarso, J., Bhatt, A.I., and Kapoor, A. (2022). PVA-based KOH polymer gel electrolyte as a membrane separator for zinc-air flow battery. Materials Today: Proceedings *64*, 1649-1654. https://doi.org/10.1016/j.matpr.2022.05.222.
66. Sun, X., Wen, Z., Liu, Y., Zhang, M., Li, W., Sheng, C., Yang, S., Zhou, H., and He, P. (2025). A Hydrogel Electrolyte-Based Zn−CO2 Battery with Improved Life. Small *21*, 2411867. https://doi.org/10.1002/smll.202411867.
67. Zhu, R., Zhu, D., Zheng, Z., and Wang, X. (2024). Tough double network hydrogels with rapid self-reinforcement and low hysteresis based on highly entangled networks. Nature Communications *15*, 1344. https://doi.org/10.1038/s41467-024-45485-8.
68. Mazloomi, K., and Gomes, C. (2012). Hydrogen as an energy carrier: Prospects and challenges. Renewable and Sustainable Energy Reviews *16*, 3024-3033. https://doi.org/10.1016/j.rser.2012.02.028.